

ALMA MATER STUDIORUM
UNIVERSITÀ DI BOLOGNA

DEPARTMENT OF PHYSICS AND ASTRONOMY "A. RIGHI"

SECOND CYCLE DEGREE

PHYSICS

A coalescence study of (anti)deuteron production in and out of jets in pp collisions at the LHC

Supervisor
Prof. Francesca Bellini

Co-supervisor
Dr. Marta Razza

Defended by
Andrea Fraternali

Graduation Session 28-29/10/2026

Academic Year 2025/2026

Abstract

The detection of antinuclei in cosmic rays would be indirect evidence of dark matter annihilation, given the orders-of-magnitude lower astrophysical background. In order to interpret measurements and develop predictions, nucleus production models and cross sections need to be constrained or directly measured in high-energy interactions at accelerator-based experiments. In particular, the coalescence mechanism, i.e. the process that binds nucleons close in phase space into nuclei, can be tested and validated. An innovative approach to perform such analysis is the study of deuteron formation in jets, where the coalescence probability should be larger due to the nucleon proximity in phase space.

This thesis develops a Monte Carlo chain to study deuteron production in jet and non-jet environments. We use `PYTHIA 8.3` as Monte Carlo event generator to simulate pp collisions at $\sqrt{s} = 13.6\,\text{TeV}$, with the help of the `FastJet` package we implement the anti-k_t algorithm for jet reconstruction and finally apply a state-of-the-art coalescence afterburner to model deuteron formation from proton-neutron pairs. As part of this work, the treatment of competing proton–neutron pairs was tested and an exclusive pairing procedure based on the coalescence weight was implemented. Deuteron spectra and the coalescence parameter B_2 are studied for jet radii R = 0.4 and 0.7 and using the Argonne v_{18} and a N^4LO χEFT wavefunction parametrization, which yield compatible results. The calculation predicts harder deuteron spectra and a substantially larger B_2 for the jet-associated component than for the non-jet component. The predicted hierarchy and order of magnitude of the in- and out-of-jet coalescence parameter are consistent with the available ALICE measurements in their measured momentum range. The results provide an important qualitative benchmark of the proposed simulation chain.

Contents

Introduction **3**

1 Search for antinuclei in cosmic radiation **4**
1.1 Cosmic rays . . . 5
1.1.1 Antimatter in primary CRs . . . 6
1.1.2 AMS-02 experiment . . . 7
1.2 Dark matter . . . 9
1.2.1 Antinuclei from WIMPs . . . 11

2 (Anti)nuclei at high energies **14**
2.1 The ALICE detector at the LHC . . . 14
2.1.1 ALICE results on light nuclei . . . 16
2.2 (Anti)deuteron production in jets . . . 20
2.2.1 ALICE results on jet deuterons . . . 21
2.2.2 Theoretical predictions on deuteron production in jets . . . 24

3 Coalescence mechanism for (anti)nucleus formation **27**
3.1 Wigner formalism . . . 28
3.2 Test of the deuteron wavefunction . . . 30
3.3 Coalescence parameter . . . 32
3.4 Alternative modeling of nucleus production . . . 33

4 Simulation tools **35**
4.1 `PYTHIA 8.3` event generation . . . 35
4.1.1 Lund String Model . . . 37
4.2 Jet reconstruction with `FastJet` . . . 38
4.2.1 Anti-k_t algorithm . . . 40
4.3 Coalescence afterburner . . . 42

5 Study of deuteron production **44**
5.1 Configuration of simulation tools . . . 44
5.1.1 `PYTHIA` tune and `FastJet` configuration . . . 44
5.1.2 Coalescence afterburner configuration . . . 46
5.2 In- and out-of-jet particle kinematics . . . 48
5.3 In- and out-of-jet deuteron production . . . 51

Conclusions **57**

Introduction

The search for light antinuclei as antideuterons and antihelium in cosmic rays has been proposed as a promising strategy for the indirect detection of dark matter, since the expected astrophysical background is orders of magnitude lower. This is especially true at low energies, below about $1 \sim$ GeV/n, where the secondary antideuteron flux, coming from interactions of primary cosmic rays with the interstellar matter, is predicted to be strongly suppressed. However, despite the large effort for dedicated space-based or balloon-borne experiments, antinuclei have never been observed in cosmic rays. Details on antimatter search in cosmic rays, dark matter annihilation and expected antideuteron flux are given in chapter 1. In order to interpret future measurements, one needs to constrain models for antinucleus production, propagation and inelastic scatterings in the Galaxy. For this reason, high-energy measurements at accelerator-based experiments are highly needed to constrain parameters for nucleus production models and measure production and scattering cross sections. In particular, in recent years, the ALICE experiment at the Large Hadron Collider (LHC) has provided multi-differential and high-precision measurements of light (anti)nuclei at midrapidity, thanks to its particle identification capabilities down to low transverse momentum. These results are reviewed in chapter 2, and include measurements of the deuteron yield in- and out-of-jets in pp and p-Pb collisions. The data from ALICE support a description of nucleus production in high-energy interactions via the coalescence mechanism, according to which final-state nucleons that are close enough in phase space can bind into a nucleus. A detailed description of the state-of-the-art Wigner-based coalescence model, with specific focus on the internal deuteron wavefunction and the coalescence parameter B_2, is given in chapter 3.

The main idea behind the present work is to test this model by studying deuteron formation in jets. There, nucleons exhibit a natural proximity in phase space, the source is potentially compact and the momentum correlations are strong. Hence, the final goal of this work is to develop and benchmark a simulation chain to study deuteron production and compare with available and future experimental results. The simulation tools we employed are described in chapter 4. They allow to generate LHC-energy pp collisions, perform jet reconstruction and simulate deuteron formation. In chapter 5, we specify our own configuration choices for the presented simulation tools and introduce our analysis. In particular, we provide a kinematical description of in- and out-of-jet particles and a study of jet-associated deuteron production. We finally report the predicted values of B_2 in and out of jets, to compare with ALICE measurements.

Chapter 1

Search for antinuclei in cosmic radiation

Around the 1920s, only the proton, the electron, and the photon were known as elementary particles. Starting in 1929, Paul Dirac developed a relativistic quantum-mechanical theory of the electron, predicting the existence of a corresponding antiparticle, namely the positron. Just a few years later, in 1932, Carl D. Anderson, while studying cosmic rays in a cloud chamber with a magnetic field, observed some particles with the same mass as the electron but opposite charge [26]: that was the first antiparticle observation. Immediately afterwards, in 1934, J. Chadwick experimentally identified a particle with a mass similar to that of the proton, though without electric charge: the neutron. Finally, in 1955, the antiproton was observed by Emilio Segrè and Owen Chamberlain at the Lawrence Berkeley National Laboratory, and the antineutron was later discovered. At that point, it was logical to think that, just like ordinary matter, antiprotons and antineutrons could form antinuclei. The simplest one, the antideuteron, was observed independently at CERN Proton Synchrotron [47] and at the Brookhaven's Alternating Gradient Synchrotron [38] in 1965.

Today, light antinuclei in cosmic rays are the subject of active experimental and theoretical research. The interpretation of their fluxes requires a quantitative description of their production and formation mechanisms, their propagation through the Galaxy, and their inelastic interactions with the interstellar medium (ISM). According to state-of-the-art models, antideuteron and antihelium can be produced by hadronic collisions between primary cosmic rays, predominantly protons, and the interstellar medium, mainly composed of hydrogen and helium. On the other hand, extensions of the Standard Model of particle physics predict the possibility of producing antimatter from dark matter, giving a new meaning to its observation.

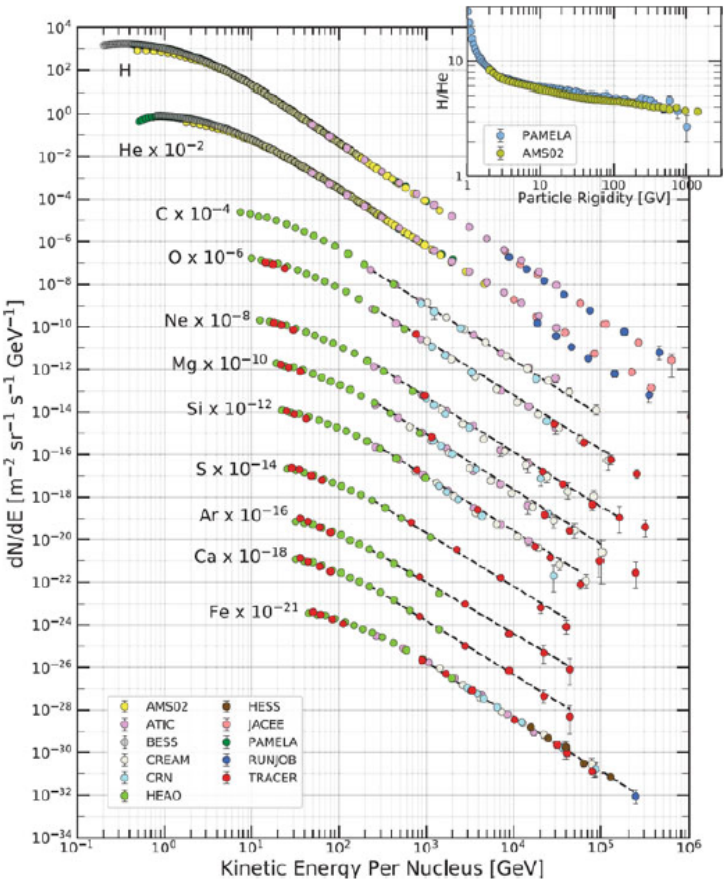


Figure 1.1: Fluxes of CR nuclei are plotted as a function of the energy per nucleus using data from direct (out of the atmosphere) experiments. For a better understanding of the figure, the flux of each nuclear species is multiplied by a scaling factor. The inset shows the H/He ratio at constant rigidity. From [59]

1.1 Cosmic rays

After the discovery of radioactivity in 1896 by Henri Becquerel it became known that some materials can produce ionizations through the emission of charged particles. These substances are called radioactive materials, for their similarity to radium (^{88}Ra). Around 1900, Wilson and others found that radioactivity was present even without radioactive elements, thus assuming the presence of background ionizing agents. The questions concerned the Earth or the extraterrestrial origin of such radiation. The final answer to the problem was given by the Austrian physicist Victor Hess. He used balloon experiments to show that the ionization, after going through a minimum, increased considerably with height. Hess concluded that the increase of the ionization originated from radiation coming from space. He also noticed the absence of day–night variations, thus excluding the Sun as the direct source of this hypothetical penetrating radiation. After the discovery of cosmic rays (CRs), a long scientific debate started about the nature of such an extraterrestrial radiation. Most believed at the beginning that cosmic rays were γ-rays, because of their huge penetrating power. In 1927, J. Clay found evidence of a variation of the cosmic ray intensity with latitude. As this deflection was attributed to the presence of the geomagnetic field, the only plausible interpretation was that the primary cosmic rays were charged particles, not

photons. Today we know that primary cosmic rays are high-energy stable particles originating in astrophysical environments. They are protons, fully ionized atomic nuclei, and electrons. However, electrons hardly escape the acceleration region, due to the emission of energy by synchrotron radiation and inverse Compton scattering. The observed composition of CRs, depending also on the propagation, is thus dominated by protons and nuclei. Part of the primary radiation can interact in (or close to) the acceleration regions, producing other high-energy charged or neutral secondary particles. Among them, photons and neutrinos are stable as well and can arrive on Earth together with the primary component. Antiparticles (mainly positrons and antiprotons) are also present in the cosmic radiation, but in most cases, they originate during the propagation of primary CRs and electrons through the galaxy. The fluxes of nuclei in cosmic radiation seem to follow a power law with a fast decrease with increasing energy. Fig.1.1 shows the major nuclear components in CRs as a function of the energy per nucleus. The power-law exponent is almost the same for all nuclear species, apart from protons. This fact is of primary importance for the theories studying the acceleration mechanisms of CRs. At the highest energies, the measurement is usually limited by statistics. The rigidity dependence of the proton and helium fluxes are important for understanding the origin, acceleration, and propagation of CRs. Precise measurements from AMS-02 show that proton and helium fluxes deviate from a single power law and progressively harden at high rigidity. The rigidity dependence is similar, as shown in the inset on the upper right in Fig.1.1.

1.1.1 Antimatter in primary CRs

The observable Universe is strongly dominated by matter, although the known microscopic laws treat matter and antimatter nearly symmetrically. The origin of the cosmological baryon asymmetry remains one of the major unknowns in cosmology and particle physics. The possible presence of cosmological antimatter in the Universe is a fundamental issue of physics, which can be addressed from the experimental point of view. Positrons in CRs had already been observed in 1964 and antiprotons in 1979, with balloon-borne magnetic spectrometers. Secondary antiprotons can be produced by CR protons interacting with ISM protons:

$$p + p \longrightarrow p + p + \overline{p} + p \tag{1.1}$$

This is the same reaction exploited in 1955 by Segrè and Chamberlain at the Berkeley Bevatron for the first antiproton observation, and occurs above the total energy threshold of $E_{thr} = 7\, m_p c^2 \simeq 6.57$ GeV for the projectile proton against the proton at rest. The corresponding kinetic energy threshold is $T_{thr} = 6\, m_p c^2 \simeq 5.63$ GeV. Being exactly the same as particles except for their opposite charge sign, antiparticles are readily distinguished, as they bend in opposite directions in the magnetic field. The antiproton-to-proton flux ratio, as a function of energy, has been measured by the three largest experiments provided with a magnetic spectrometer: BESS [19], PAMELA [51] and AMS-02 [24]. The measured antiproton spectrum agrees with detailed theoretical simulations that assume pure secondary production of antiprotons during the propagation of primary CRs in the Galaxy and in-

teractions with the interstellar medium [31]. For positrons, the observed spectrum can be explained by secondary production only at low energy. At higher energies, measurements of the positron flux and positron fraction show an excess with respect to predictions based solely on secondary production, suggesting the presence of an additional component of astrophysical or possibly exotic origin [25].

No antinuclei heavier than antiprotons have been detected so far in CRs. The BESS experiment provides the lowest upper limit to date on the relative antihelium-to-helium ratio, 6.9×10^{-8}, within the rigidity range 1–14 GV [2]. BESS also provides the lowest upper limit for the antideuteron flux of $6.7 \times 10^{-5} (\mathrm{m^2\,s\,sr\,GeV/n})^{-1}$ at the 95% confidence level, between 0.16 and 1.1 GeV/n [53]. The detection of even a few antideuteron or antihelium nuclei would help to constrain the mechanisms of antinuclei production and propagation in the Galaxy, as well as shed light on possible exotic sources. Indeed, several new physics scenarios predict antideuteron or antihelium fluxes significantly larger than the one expected from cosmic ray collisions, thus providing a potential "smoking gun" for exotic phenomena in our Galaxy, such as the nature of dark matter (DM).

However, interpreting these measurements requires a good understanding of all involved processes to distinguish potential exotic contributions from ordinary production. For example, the production and absorption cross-sections of antinuclei need to be provided by accelerator-based experiments [9], such as those conducted at the Large Hadron Collider (LHC); the transport and propagation of the produced antinuclei through the Galaxy and the influence of the magnetic fields of the Sun and Earth need to be benchmarked by nuclei measurements in space [52].

1.1.2 AMS-02 experiment

AMS-02 [24] is a large-acceptance magnetic spectrometer installed on the International Space Station (ISS) since 2011 and designed for precision measurements of the composition and fluxes of charged cosmic rays. It could open new information on the Universe and its origin by searching for antimatter and, indirectly, for dark matter. AMS-02 uses a very large permanent magnet (which is the heart of the detector) operating at ambient temperature. The configuration of the magnet has a negligible net dipole moment to avoid coupling with the Earth's magnetic field, which would disturb the orbit of the ISS.

Inside the magnet, the central tracker can precisely measure the curvature of the particles traversing the magnet and determine the particle rigidity. The tracker records the coordinates of a particle at eight different positions with a precision of ~ 10 μm at each point. The radius of the best circular trajectory passing through the points defines the particle curvature, used to evaluate the rigidity and so the charge sign.

The time of flight (TOF) system can measure the particle transit time through the detector and provide triggers for the other subdetectors. Since the distance between the upper and lower TOF planes is approximately 1.2 m, the TOF can resolve particle velocities up to 0.98 times the speed of light in vacuum. It is composed of four planes of scintillation counters, two above and two below the magnet. The scintillators are coupled at both ends

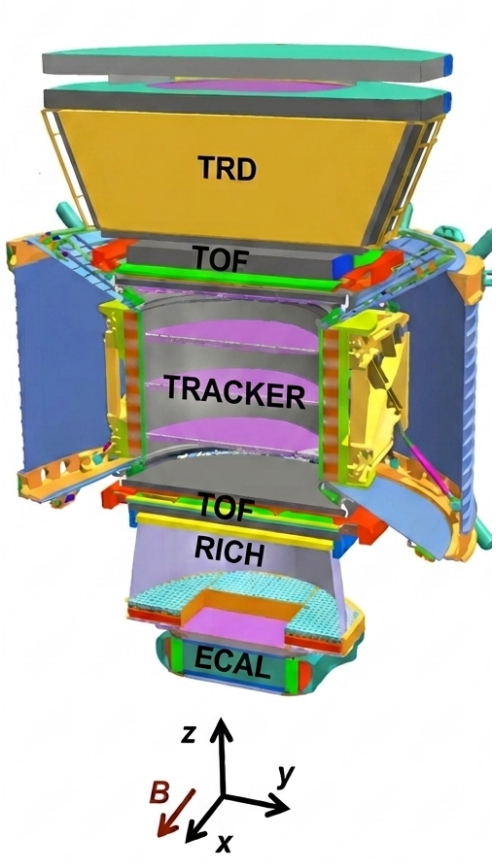


Figure 1.2: Structure of the AMS-02 detector with the main components, from top to bottom: the Transition Radiation Detector (TRD), the Time of Flight counter, the tracker, the Cherenkov counter (RICH), and the electromagnetic calorimeter. Modified from [24]

via light guides to photomultipliers. The TOF system is also important for antimatter discrimination, as it can discriminate up-going and down-going particles with a rejection factor of 10^{-9}. In a magnetic field, the trajectory of an upward-going electron is equivalent to that of a downward-going positron, and a wrong assignment of the direction would induce a wrong charge assignment. Together with the tracker, the TOF can also provide the charge modulus, while the measurement of velocity is complemented by a Cherenkov counter (RICH). By considering also the rigidity, one can compute the mass and thus identify the nucleus.

Finally, a Transition Radiation Detector (TRD) provides an independent measurement of the Lorentz factor and is primarily used to discriminate electrons and positrons from the much larger hadronic background.

This experiment provided the most precise antiproton spectrum in the range 1-450 GV [31]. In 2018, the Collaboration also announced a few candidate events [62] with mass and charge consistent with antihelium, six $^3\overline{\text{He}}$ and two $^4\overline{\text{He}}$, which, however, have not been confirmed to date.

1.2 Dark matter

Most of the information about our Galaxy, as well as the rest of the Universe, comes from electromagnetic emission: not only in the optical band, but also in the radio, infrared, X-ray, and γ-ray bands. The existence of matter in the Universe that does not emit electromagnetic radiation, dark matter, was inferred through its gravitational interaction with ordinary matter, which does emit electromagnetic radiation.

The first hints of the presence of dark matter were observed in 1933 by Zwicky from measurements of the velocity dispersion of the galaxies in the Coma Cluster. He estimated its total mass using the brightness of visible galaxies, as well as the radial velocities from the Doppler shift of emitted light. Zwicky found that the individual galaxies within the cluster were moving too fast for the cluster to remain stable [66]. To explain this, he proposed the existence of an invisible mass, which he called dark matter, exerting gravitational attraction without emitting light. He derived a mass-to-light ratio of around 400 solar masses per unit of solar luminosity, which exceeds that observed in the solar neighbourhood by two orders of magnitude.

Evidence for dark matter is obtained across a wide range of astrophysical and cosmological scales, including galaxy rotation curves, the dynamics and gravitational lensing of galaxy clusters, cosmic-microwave-background anisotropies and large-scale structure formation. The analysis of the revolution speeds of stars and gas clouds in the galactic halo as a function of the distance from the center of the galaxy provides one of the most straightforward observational indications for the presence of dark matter [63]. We can consider, for example, a spiral galaxy, where the revolution speed of a mass m star around the center is given by the equality of gravitational and centrifugal force:

$$\frac{GM_r m}{r^2} = \frac{mv^2}{r} \tag{1.2}$$

from which

$$v(r) = \sqrt{\frac{GM_r}{r}} \tag{1.3}$$

where M_r is the total mass included within a distance r from the center of the galaxy. Most of the stars of a spiral galaxy are located in the central spherical bulge with radius r_b. If $\bar{\rho}$ is the average density of stars in the bulge, we have that

$$v(r) = \sqrt{\frac{4}{3}\pi G\bar{\rho}} \cdot r \propto r \quad \text{for} \quad r < r_b \tag{1.4}$$

while

$$v(r) \propto \frac{1}{\sqrt{r}} \quad \text{for} \quad r > r_b \tag{1.5}$$

If we assume all the galaxy mass lies inside the bulge. Using the 21-cm hydrogen emission line, the circular velocities of neutral hydrogen clouds can be measured as a function of r. In almost all cases, after a rise near $r = 0$, the velocities remain constant as far as can be

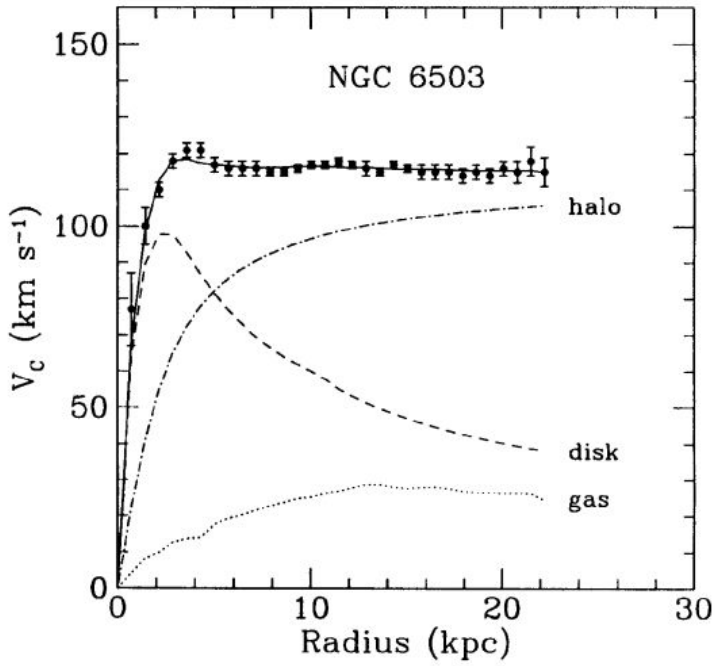


Figure 1.3: One of the historical plots for rotation curves of spiral galaxies. It shows disk and gas contributions, in addition to the dark matter halo needed to fit the data. From [40]

measured, as shown in the famous plot in Fig.1.3 for the spiral galaxy NGC 6503. The luminous mass is gathered within a distance of about 5 kpc from the center of the galaxy, but stars keep an unexpectedly large revolution speed as measured using the Doppler effect. The figure also shows the contribution of a possible dark matter halo, which is necessary to explain the observed data. It is evident indeed that at high r, the measured velocities are larger than those obtained using Eq.(1.3), also including the additional contribution of stars and gas in the disk. Similar results are obtained by measuring the speed of stars in other spiral galaxies and in elliptical galaxies.

Several hypotheses have been proposed in the past to clarify the particle nature of DM and to suggest possible searches. Possible candidates are sterile neutrinos, hypothetical particles that are singlets under all Standard Model interactions. They also have right-handed chirality, in contrast with the known "active" neutrinos that couple with the Z^0 and $W^{\pm}$ bosons in the Standard Model.

The Weakly Interacting Massive Particles (WIMPs) represent the dark matter candidates that have historically received greater attention. In the following, we will mainly focus on this class of candidates. They are colorless, electrically neutral, stable particles that arise in some extensions of the Standard Model. Thus, they interact with ordinary matter only through weak interactions, in addition to gravity. Predicted WIMP masses are within the range from 10 GeV to a few TeV (in natural units). A notable example could be found in a supersymmetric extension of the Standard Model, with the so-called neutralino (denoted by χ) being a WIMP candidate [49].

1.2.1 Antinuclei from WIMPs

If dark matter was in thermal equilibrium in the early Universe, and froze out when the temperature dropped due to expansion, it is a natural assumption that WIMPs can interact with each other and produce Standard Model particles. Otherwise, they would not have annihilated in the early Universe and would be unacceptably overabundant today.

All dominant annihilation processes for neutralinos are characterized by two-body final states: $q\overline{q}$, W^+W^-, Z^0Z^0, two Higgs bosons, one ordinary gauge boson and a Higgs boson. In quark final states, the produced quarks and antiquarks initiate parton showers, followed by hadronization, which gives rise to a large number of hadrons, including antinucleons. For bosonic final states, the corresponding bosons first decay, with their hadronic decay products subsequently undergoing parton showering and hadronization. The resulting antiprotons and antineutrons can then form antideuterons through the coalescence process if they are close enough in phase space.

For neutralino masses below the threshold for annihilation into massive gauge bosons, fermion–antifermion ($f\overline{f}$) final states can constitute the dominant accessible two-body channels [59]. One important feature of this channel is the helicity constraint. Neutralinos are Majorana fermions and in the limit of zero relative velocity they are in a relative s-wave (i.e. null relative orbital angular momentum). Consequently, by Fermi statistics, they must have spins oppositely directed, so that the total angular momentum is null. Therefore, the two fermions in the final state must have oppositely directed spins as well. This configuration introduces a helicity factor in the probability amplitude that is proportional to the mass of the fermion m_f, analogously to the decay of the charged pion. In the low-energy limit, we can consider a point-like interaction described by the effective Lagrangian:

$$\mathcal{L} = \frac{1}{\Lambda^2}(\overline{\chi}\gamma^\mu\gamma^5\chi)(\overline{f}\gamma_\mu\gamma^5 f) \tag{1.6}$$

where Λ is a suppression energy scale characterizing the process (for example, we could take $\Lambda = 2m_\chi$). We can then compute the probability for the process, which is proportional to the squared amplitude:

$$\sum_{spins} |\mathcal{M}|^2 \propto \frac{m_\chi^2 m_f^2}{\Lambda^4} \tag{1.7}$$

Thus, neutralinos preferentially annihilate into the highest mass accessible fermions: annihilation into light quarks and leptons is suppressed in comparison with heavy quarks (i.e. b and t) and the τ lepton. Direct decay into massless particles is forbidden (and that into neutrino thus completely negligible). However, branching ratios for different channels are of course model-dependent.

The production of stable Standard Model particles in WIMP annihilation provides the basis for indirect dark-matter searches. The latter relies on the possibility of detecting γ-rays, neutrinos, or charged particles resulting from WIMP annihilation. This is an additional, although subdominant, contribution to the cosmic radiation from astrophysical

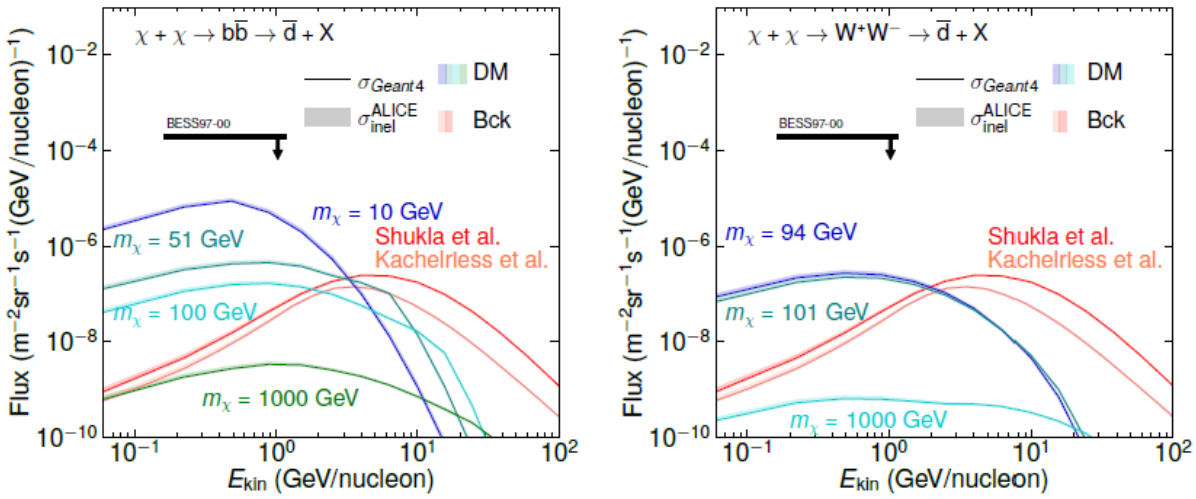


Figure 1.4: Antideuteron fluxes from cosmic-ray collisions with the interstellar medium (red and orange) and for two different production scenarios ($b\bar{b}$ at left and W^+W^- at right) from dark-matter annihilation expected at Earth. Antideuteron spectra from DM are predicted for several WIMP masses (blue and green curves). From [56]

origin. Typical dark matter models are, however, democratic in producing as much matter as antimatter in the annihilation or decay final products [59]. Since antimatter is not abundant as primary radiation, the search for stable antiparticles in primary CRs is a promising method for searching for a possible DM signal. However, antiprotons and antinuclei can also be produced by high-energy protons and helium nuclei interacting with the ISM, hence yielding backgrounds against which a potential DM signal is to be searched in the form of a spectral excess.

Predicted antideuteron spectra at Earth [56] are shown in Fig.1.4. Two different sources are considered, in particular dark-matter annihilation into $b\bar{b}$ (left) and W^+W^- (right), for several WIMP masses. Fiducial values for source and propagation parameters are used. The horizontal black line shows the upper limit for the antideuteron flux obtained by the BESS experiment, already mentioned in subsection 1.1.1. Both panels also show the secondary antideuteron flux produced in the collisions of cosmic rays in the interstellar medium, computed with two different coalescence models (red and orange curves). Figure 1.4 leads to the well-known conclusion that low-energy antideuterons ($E_{kin} < 1$ GeV/nucleon) can exhibit a large signal-to-background ratio between exotic sources of antinuclei and secondary antideuterons. Compared with antiproton production, secondary antideuteron production has a higher effective threshold because an antiproton and an antineutron must first be produced and must then emerge sufficiently close in phase space to form a bound state. This strongly suppresses the low-energy secondary antideuteron flux and makes the modelling of coalescence a central ingredient of the background prediction (see chapter 3). The strong suppression of the conventional low-energy component makes this region particularly sensitive to an additional contribution from exotic sources. A sta-

tistically significant excess over the predicted secondary flux would therefore provide an important signature to investigate. The properties of light cosmic-ray antinuclei have been studied in accelerator-based experiments using various colliding systems and colliding energies to determine their production and propagation mechanisms quantitatively [13][17]. The required measurements include, for example, antinuclei production and baryonic femtoscopy experiments in pp and p-A interactions in the forward direction at energies of the order of tens of GeV [21]. For collider-based experiments, antinuclei studies pose three challenges to address:

- measuring the antinucleus production in Standard Model collisions, to understand the formation process and constrain coalescence models;
- studying the inelastic interaction of antinuclei with matter particles to determine the Galaxy's transparency;
- providing data to calibrate event generators for both secondary cosmic-ray interactions and dark-matter annihilations or decays.

Despite of the plethora of very precise measurements, the studies do not suffice to constrain the antinucleus production and propagation cross sections within the very wide energy range of collisions occurring between high-energy cosmic rays and nuclei present in the interstellar medium, going from a center-of-mass energy threshold of about $\sqrt{s} \simeq 6\,\mathrm{GeV}$ up to hundreds of TeV, with the largest contribution to the antideuteron yield coming from cosmic ray energies around 300 GeV [56]. Hence, relatively large uncertainties are still present in the most critical energy region, i.e. below 100 GeV [41].

Chapter 2

(Anti)nuclei at high energies

The study of how (anti)nuclei are formed is interesting from different points of view, not only for the understanding of the formation mechanism, but also for astrophysical aspects. Therefore, empirical data at energies relevant to cosmic ray interactions are highly needed if we aim to understand the expected astrophysical backgrounds. In past years, numerous heavy-ion collision data have been analysed at the Relativistic Heavy Ion Collider (RHIC) and at the Large Hadron Collider (LHC). With the data from the first RHIC operation in 2000, the STAR collaboration measured the production of antideuterons [18]. Later, the collaboration extended such studies to $A \geq 2$, reporting eventually the discovery of the first antimatter hypernucleus [60] and the observation of $^4\overline{\mathrm{He}}$ [61]. More recently, the versatility of both the Large Hadron Collider and the ALICE (A Large Ion Collider Experiment) apparatus has given additional access to a unique set of nuclear and hadronic physics measurements also in small colliding systems such as pp and p-Pb collisions. Small colliding systems are most relevant for studying antinuclei production by cosmic-ray interactions in the ISM. Collider measurements do not reproduce the full fixed-target kinematics of cosmic-ray interactions, which particularly requires data in the forward region and over a broad energy range. They nevertheless provide essential constraints on antinucleon production, correlations, and coalescence models used to extrapolate to astrophysical conditions.

2.1 The ALICE detector at the LHC

A Large Ion Collider Experiment (ALICE) [5] is a dedicated heavy-ion collision experiment located at the LHC. In this discussion, we refer to the Run 2 configuration [1], shown in Fig.2.1. The experiment aims to investigate the properties of the Quark-Gluon Plasma (QGP), a state of matter characterized by a hot and dense environment where quarks and gluons are no longer confined. This plasma is believed to have existed in the early moments after the Big Bang and is recreated in high-energy heavy-ion collisions [4]. ALICE research is not limited to heavy-ion collisions like lead-lead (Pb-Pb) but also includes proton-proton (pp) collisions. ALICE is equipped with sophisticated particle identification systems and advanced tracking capabilities that can operate in high-multiplicity

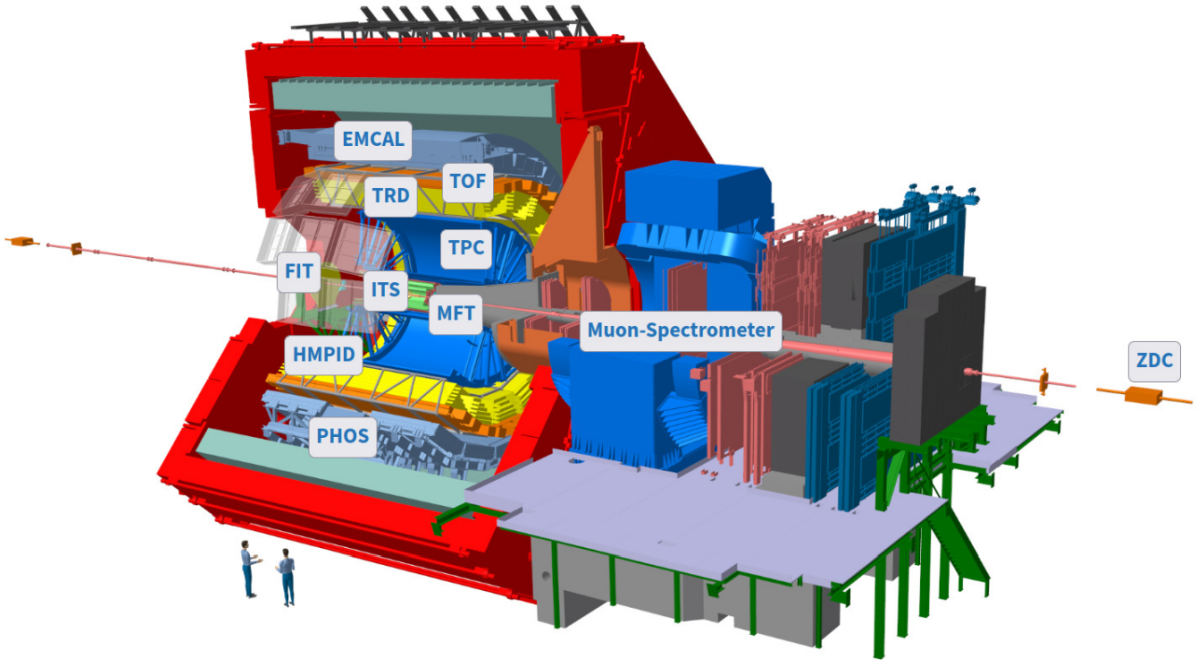


Figure 2.1: Overview of the ALICE detector. From [1]

environments and detect particles at low momenta. The ALICE detector is equipped for studying the interactions of heavy quarks (charm and bottom) and the thermal radiation emitted from the QGP using dielectron measurements. Additionally, ALICE provides high-precision measurements in collective flow and hydrodynamic properties of the medium, jet quenching phenomena, particle production, and hadron-hadron interactions, as well as collective effects in high-multiplicity pp collisions. Thanks to its particle identification capabilities down to very low transverse momentum, ALICE is complementary to the other LHC experiments in this field.

ALICE comprises various subdetectors that provide complementary information on the particles produced in heavy-ion collisions, allowing for the reconstruction of the collision vertex and the tracking and identification of the produced particles. They are divided into a central barrel, housing a solenoidal magnet with a magnetic field of 0.5 T, and forward detectors. The main components of ALICE include:

- Inner Tracking System (ITS): the detector closest to the interaction point. Its primary objective is to reconstruct the primary vertex of the collision, track and identify low-momentum particles, reconstruct secondary vertices resulting from long-lifetime particle decays and separate primary and secondary tracks through the distance of closest approach to the primary vertex.

- Time Projection Chamber (TPC): cylindrical gas detector used for central-barrel tracking and charged-particle identification through their specific ionisation energy loss. The track curvature in the solenoidal magnetic field is used to determine the

momentum and charge sign.

- Time of Flight (TOF): identifies particles by measuring their time of flight, used to compute the velocity (β).
- Transition Radiation Detector (TRD): helps reconstruct charged particles within $|\eta| < 0.9$, allows event triggering, and differentiates electrons from background pions.
- Electromagnetic Calorimeter (EMCal): detects high-energy photons and electrons, especially from decays of hadrons or neutral mesons.
- Photon Spectrometer (PHOS): provides precise measurements of photons with high spatial and energy resolution.
- High Momentum Particle Identification Detector (HMPID): uses Cherenkov radiation to identify hadrons at large transverse momentum.
- Muon Spectrometer: detects muons from hadronic decays within the pseudorapidity range $-4 < \eta < -2.45$.

2.1.1 ALICE results on light nuclei

Besides being at the forefront in the study of the QGP evolution and its properties, in recent years the ALICE experiment has demonstrated to be uniquely sensitive to specific aspects of low-energy nuclear and hadronic physics. At LHC energies, the baryochemical potential, the thermodynamic parameter associated with baryon-number conservation and the control of the relative abundance of baryons and antibaryons in the system, is close to zero at midrapidity, leading to nearly equal production yields of nuclei and antinuclei. This matter-antimatter symmetry at LHC energies allows for the study of production yields and of elastic and inelastic interaction cross sections with the detector materials of light nuclei and antinuclei at the same time [21]. The production of (anti)deuteron, (anti)triton, (anti)^{3}He, (anti)^{4}He and even (anti)hypertriton ($^3_\Lambda$H) nuclei have been studied in several collision systems, providing a solid test for microscopic models of (anti)nucleus production and their inelastic interactions.

A detailed understanding of the formation of light (anti)nuclei and hypernuclei has been achieved by investigating their production as a function of the system size. In small collision systems, such as pp or p–Pb, the nucleon-emitting source radius is about 1-2 fm [14]. The size of the source is thus smaller than (or similar to) the size of the (anti)nuclei that are formed from it, as for instance the RMS charge radius of the deuteron is 2.14 fm. In large collision systems like Pb–Pb collisions, the opposite is true, as the radius of the emitting source is about 4–9 fm [16].

The measured yields of (anti)nuclei relative to those of protons as a function of $\langle dN_{ch}/d\eta \rangle$ are summarized in the left panel of Fig.2.2. Similarly to other light-flavoured hadrons, a smooth trend with $\langle dN_{ch}/d\eta \rangle$ across different collision systems is observed. Also, near-multiplicity measurements show independence of the centre-of-mass energy, within the

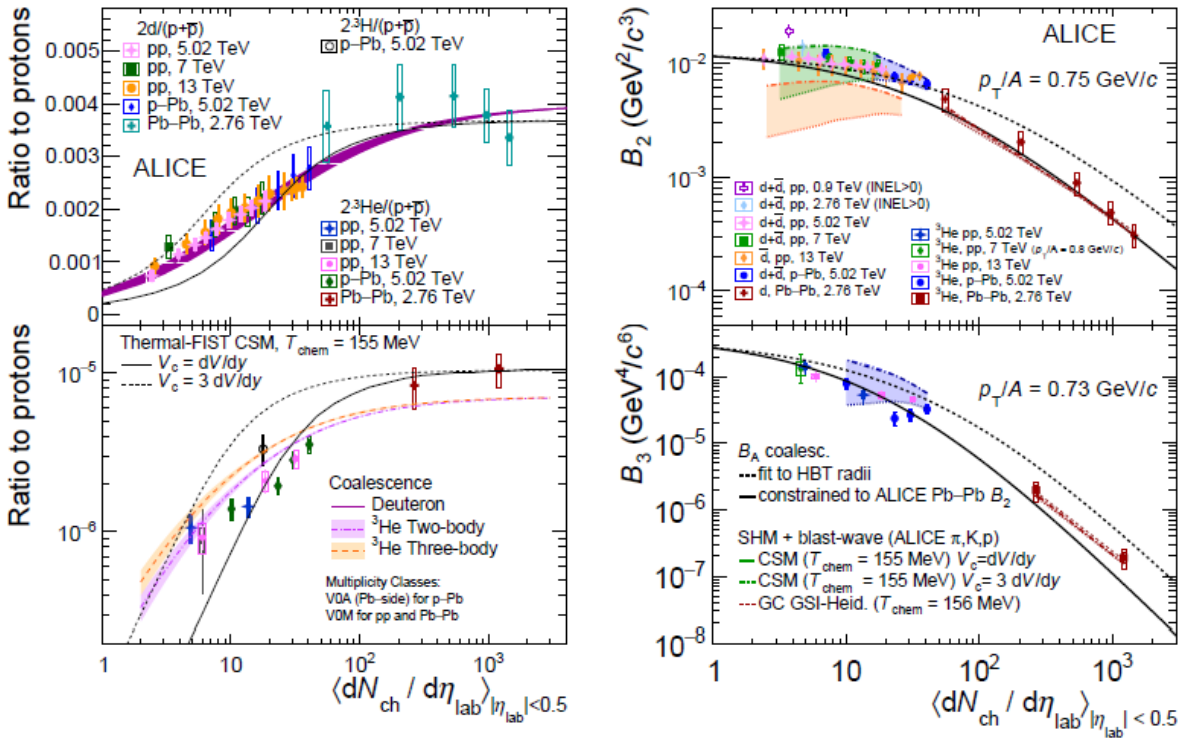


Figure 2.2: (Left) d/p ratio (Top) and 3He/p ratio (Bottom) in pp, p–Pb, and Pb–Pb collisions as a function of the mean charged-particle pseudorapidity density. (Right) Coalescence parameters B_2 (Top) and B_3 (Bottom) as a function of the mean charged-particle pseudorapidity density for pT/A = 0.75 GeV/c (0.73 GeV/c) calculated using the average of particles and antiparticles. In all panels, the expectations for the canonical statistical hadronisation model (SHM) evaluated with Thermal-FIST and coalescence approaches are shown. The uncertainties of the coalescence calculations, which are due to the theoretical uncertainties on the emission source radius, are denoted as shaded bands. From [4]

known uncertainties. The nucleus-to-proton ratios exhibit an increasing trend with increasing multiplicity for low-$\langle dN_{ch}/d\eta \rangle$, and they tend to saturate for $\langle dN_{ch}/d\eta \rangle \gtrsim 100$. The yield ratios at high multiplicity are in good agreement with predictions from statistical hadronisation models (SHMs). In these models, the production yield per unit of rapidity of a given particle species is mostly determined by the chemical freeze-out temperature (T_{chem}) and the particle mass, with an approximately exponential dependence. Besides SHMs, data in the left panel of Fig. 2.2 are also compared to predictions from a coalescence model for nucleus production (see chapter 3).

Also, the dependence of the coalescence parameter B_A (i.e., the probability of nucleus formation) at a given value of p_T/A on the event multiplicity is shown in the right panel of Fig.2.2 for deuteron and ^{3}He. A strong decrease with increasing multiplicity is observed for both B_2 and B_3; this is explained in the coalescence model by an inverse proportionality to the source volume: the coalescence probability of two or three nucleons is suppressed

if they are largely separated in configuration space. This effect becomes less apparent in small collision systems where the size of the produced nucleus is larger than the source size. In general, the measured yields of light nuclei and their multiplicity dependence across different collision systems can be qualitatively described by the SHM for particle production at the chemical freeze-out and by the coalescence of nucleons at the kinetic freeze-out, even though some open questions still need to be addressed. Integrated yields and coalescence parameters alone have not provided an unambiguous discrimination between microscopic production scenarios. More differential observables, such as pion-deuteron correlations, have recently supplied direct information on whether deuterons are assembled from nucleons produced in resonance decays.

Femtoscopy provides a complementary approach to investigate the microscopic processes underlying (anti)deuteron formation by examining pion-(anti)deuteron (π–d) momentum correlation. In fact, as a bound state of a proton and a neutron, the deuteron may inherit correlations developed by its constituent nucleons during the evolution of the collision. If deuterons are produced thermally alongside pions, any correlation signal between them would arise solely from final-state interactions. In contrast, if deuterons form through the coalescence of nucleons originating from the decay of an intermediate resonance (together with pions), the resulting π–d correlation function could retain the signature of that resonance.

A recent ALICE study [3] takes into account different scenarios, in which pions and deuterons are produced following a SHM or by Δ-resonance decays. The Δ resonances are very short-lived excited states of nucleons, with a lifetime of approximately 1.5 fm, and predominantly decay into a pion and a nucleon. These decays therefore provide an additional source of protons and neutrons that can participate in deuteron formation. In the coalescence picture, a nucleon produced in a Δ decay can combine with another nearby nucleon, provided that they are sufficiently close in phase space. For example, the proton produced in $\Delta^{++} \rightarrow \pi^+ p$ or $\Delta^0 \rightarrow \pi^- p$ can coalesce with a neutron, while a neutron produced in $\Delta^+ \rightarrow \pi^+ n$ or $\Delta^- \rightarrow \pi^- n$ can coalesce with a proton. This scenario was simulated by exploiting the state-of-the-art coalescence afterburner described in chapter 3, combined with the EPOS 3 event generator.

The correlation function $C(k^*)$ is the key experimental observable, and k^* is the single-particle momentum in the pair rest frame (PRF). Experimentally,

$$C(k^*) = \mathcal{N} \frac{N_{same}(k^*)}{N_{mixed}(k^*)}, \tag{2.1}$$

where $N_{same}(k^*)$ (same-event sample) is the distribution of relative momenta between the π–d pair measured for pions and deuterons stemming from the same collision [12]. Equivalently, $N_{mixed}(k^*)$ (mixed-event sample) is an uncorrelated reference obtained via the combination of pions and deuterons originating from different collisions. Lastly, $\mathcal{N}$ is a normalization factor ensuring the proper convergence of the function to unity at large k^*. Indeed, in the case of non-interacting particles, the correlation function is equal to unity for all k^*, as the relative momentum distribution is purely governed by the underlying single-particle phase space, which is the same for the two distributions. An attractive

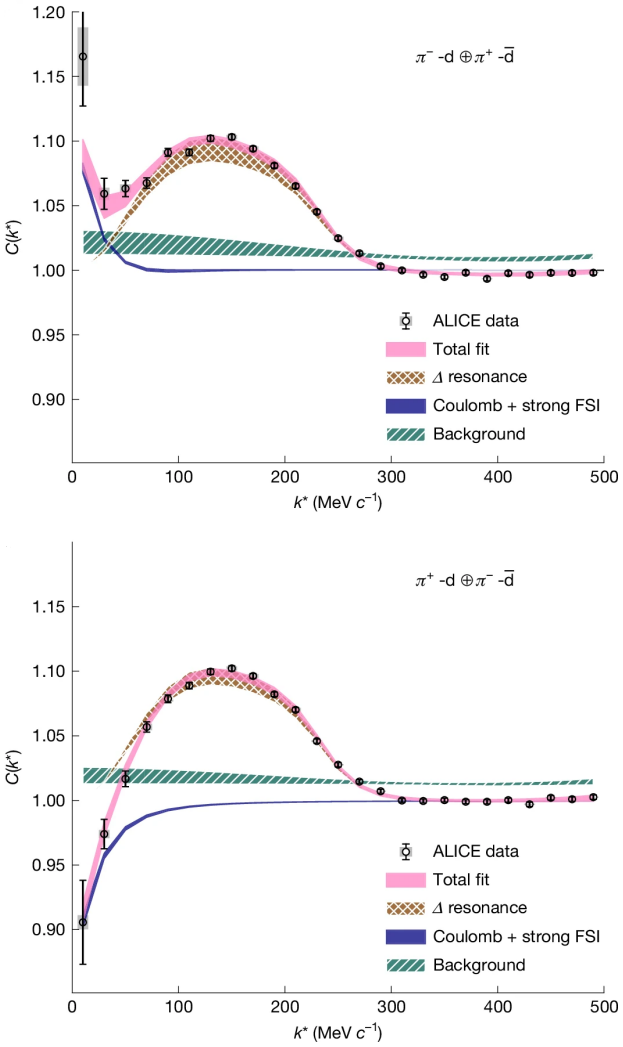


Figure 2.3: Experimental π^-–d and π^+–d correlation functions. The data are obtained from high-multiplicity pp collisions at $\sqrt{s} = 13$ TeV. The measured correlation function is shown together with the corresponding fit function (magenta). The brown cross-hatched band represents contributions from the Δ resonance, the blue band denotes the Coulomb and strong final-state interactions, and the teal diagonally hatched band corresponds to the residual background. The widths of the bands indicate the fit uncertainty. From [3]

interaction enhances the correlation function above unity at low $k^* \leq 200\,\text{MeV}$, while a repulsive interaction leads to a depletion below unity. A resonance which decays into the hadron pair of interest would produce a peak in the k^* spectrum. A clear peak compatible with the Δ nominal mass is thus expected in the correlation function, due to the residual correlation between the pion and an (anti)nucleon from the Δ decay during the (anti)deuteron formation process. The experimental π^+–d and π^-–d correlation functions have been measured in pp collisions at $\sqrt{s} = 13$ TeV [3] and are shown in Fig.2.3. Since the same interaction governs hadron–hadron and antihadron–antihadron pairs, the sum of particles and antiparticles is considered. Within the correlation model used in [3], the data favour a scenario in which a substantial fraction of deuterons and antideuterons is formed by the coalescence of nucleons originating from strong-resonance decays. The residual signal in the π–d correlations can be used to evaluate the fraction of (anti)deuterons produced following Δ decays, which is found to be $60.6 \pm 4.1\%$. Extending this reasoning to all strong resonances produced in pp collisions at $\sqrt{s} = 13$ TeV, it is found that

$88.9 \pm 6.3\%$ of (anti)deuterons are formed through binding processes involving nucleons originating from strongly decaying resonances. This large fraction demonstrates that most of the (anti)nuclei are produced through secondary binding processes in pp collisions at the LHC and not by direct emission as other hadrons.

2.2 (Anti)deuteron production in jets

An innovative approach that can help to clarify the mechanism of nucleus formation is the study of the production of nuclei inside and outside of jets. Jets are collimated beams of particles originating from the fragmentation of quarks or gluons in high-energy processes. Hadrons in the jet cone are closer in phase space compared with hadrons out of the jet. In a jet fragmentation, the produced particles are strongly correlated in phase space, i.e. particles which are close in space have also similar momenta. In the coalescence picture, this condition should result in a larger coalescence probability in jets compared with that in the underlying event (UE), since the proximity in both space and momentum is required for coalescence. This study has been performed in pp collisions at $\sqrt{s} = 13$ TeV [6] and in p–Pb collisions at $\sqrt{s_{NN}} = 5.02$ TeV [20]. In these studies, due to the limited data sample available, the jet is not fully reconstructed using jet finder algorithms, but a classification in terms of the angular distribution is employed. In particular, the particle with the highest transverse momentum, and also higher with respect to a given threshold, is used as a proxy for the jet axis. To this particle, an azimuthal angle $\phi_0 = 0$ is assigned. All other particles produced in the collision are classified in three different azimuthal regions, according to the $\Delta\phi = |\phi - \phi_0|$ value, precisely:

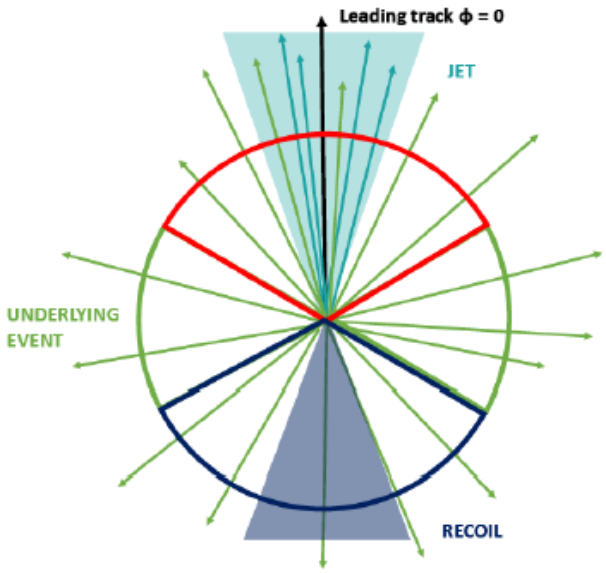


Figure 2.4: Schematic view of the azimuthal regions.

- Toward: $\Delta\phi < 60°$, containing both jet contribution and UE;
- Away: $\Delta\phi > 120°$, back-to-back to the Toward one, contains the recoil jet and the UE;
- Transverse: $60° < \Delta\phi < 120°$, characterized by the UE.

A schematic representation of such regions is reported in Fig. 2.4. The jet-associated yield is estimated as the difference between the Toward and Transverse yields, exploiting their equal azimuthal widths and assuming that the Transverse region provides an unbiased estimate of the underlying-event contribution in the Toward region.

2.2.1 ALICE results on jet deuterons

Deuteron production in jets was measured in pp collisions at $\sqrt{s} = 13$ TeV by the ALICE Collaboration using the two-particle correlation method [8]. More recently, also (anti)deuteron coalescence parameters in jet-associated events have been measured for the first time [6]. Deuteron candidates are selected from charged-particle tracks reconstructed in the Inner Tracking System (ITS) and Time Projection Chamber (TPC) in the pseudorapidity interval $|\eta| < 0.8$. Basic track quality criteria are applied, e.g., a selection on the number of space points associated with the track in the TPC and ITS and on the χ^2 of the track fit, as done in previous light (anti)nucleus analyses. The particle identification is complemented by the Time of Flight (TOF) system. The raw (anti)deuteron p_T spectra are corrected for the reconstruction efficiency and, only for deuterons, for the fraction of secondary deuterons produced by spallation in interactions between primary particles and the detector material. The dominant contributions to the systematic uncertainties are related to the track selection, the particle identification, the limited knowledge of the ALICE material budget, the uncertainties on the hadronic interaction cross section of (anti)deuterons, and the procedure used to estimate the fraction of secondary nuclei.

The average of the deuteron and antideuteron p_T distributions measured in the three azimuthal regions discussed above is shown in Fig. 2.5 left. The p_T spectrum of (anti)deuterons in jets is obtained by the subtraction method. The resulting spectrum, with a much harder shape compared to the UE spectrum, is shown in Fig. 2.5 right, with squared markers, and compared to the in-jet deuteron spectrum measured with the two-particle correlation method taken from [8]. Within the experimental uncertainties, the spectrum obtained with the subtraction method is consistent with the earlier two-particle-correlation result, providing an important validation of the jet-associated yield extraction. These results confirm that the integrated yield of deuterons in jets, in events with a threshold for the leading track at $p_T > 5$ GeV/c at midrapidity, is only roughly 10% of that in the UE, as already pointed out in [8].

A similar analysis has been performed in p-Pb collisions at $\sqrt{s_{NN}} = 5.02$ TeV [20]. The two systems differ in some aspects, such as spatial dimension and multiplicity of charged particles. Specifically, the source size, i.e. the region that emits hadrons with

similar momenta, in p–Pb is slightly larger with respect to the pp case. In this case, the coalescence model predicts a smaller coalescence probability out of jets in p–Pb collisions with respect to the same quantity evaluated in pp collisions. It is important to note that the results of this analysis may depend on how the jets are defined, i.e. whether a trigger particle of a given p_T or the full p_T of the jet is considered. For this reason, the same jet definition used in pp collisions is applied to allow for a comparison. The p_T distributions of the average of deuteron and antideuteron in the three azimuthal regions are shown in Fig.

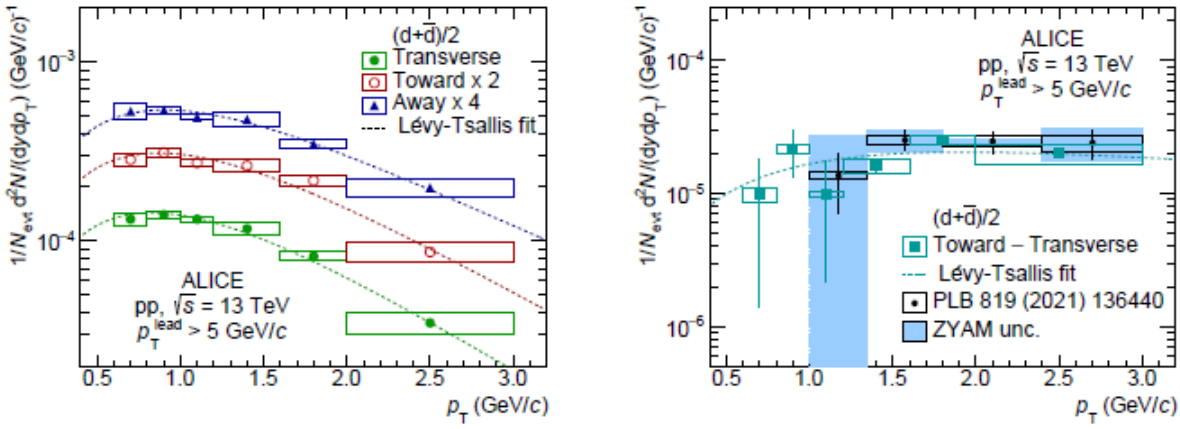


Figure 2.5: Average of deuteron and antideuteron pT-differential yields in the three azimuthal regions (on the left) and in jets (on the right), measured in pp collisions at $\sqrt{s}$ = 13 TeV. Statistical and systematic uncertainties are represented by vertical bars and boxes, respectively. On the right, shaded (blue) boxes show the uncertainty on the results from [8]. Individual Lévy-Tsallis fits are also shown. From [6]

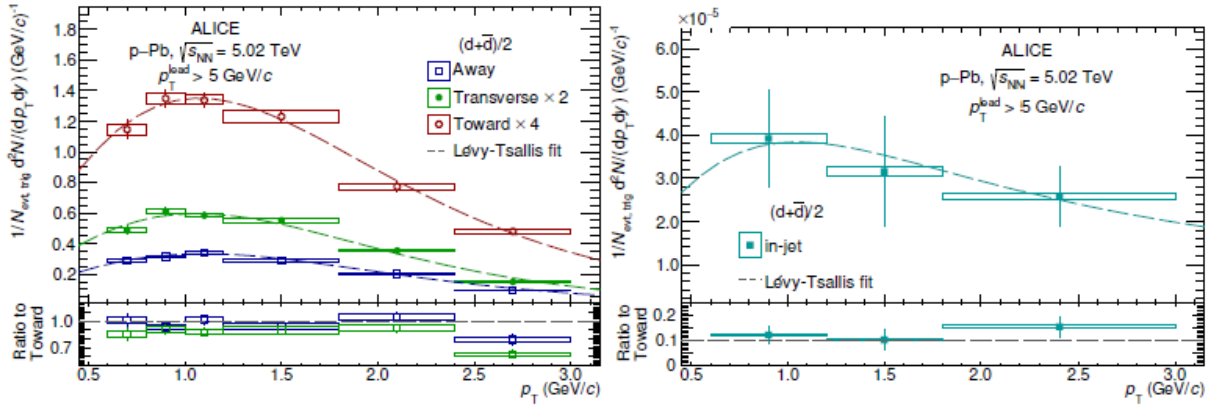


Figure 2.6: The average of deuteron and antideuteron p_T-differential yields in the three azimuthal regions (left) and in jets (right) measured in p–Pb collisions at $\sqrt{s_{NN}}$ = 5.02 TeV. Statistical and systematic uncertainties are reported, respectively, with vertical lines and boxes. Individual Lévy-Tsallis fits are also shown. The distributions are scaled for visibility reasons. The bottom panel of each figure shows the ratio of the distribution with respect to the Toward one. From [20]

2.6 (left). The transverse-momentum distributions in the Toward and Away regions are compatible, while the Transverse is about 90% of the Toward region. As already observed in pp collisions, the jet contribution accounts for only about 10% of the total particle production in the Toward region. Hence, with the jet definition adopted in this analysis, the Toward region is also dominated by the underlying event. Moreover, as expected in the case of the jet-associated particle production, the distributions in jets show a hardening with respect to the ones out of jets.

The coalescence parameter in and out of jets is calculated using the expression

$$B_2 = \left(\frac{3}{2\pi P_T}\frac{d^2N_d}{dydP_T}\right) \Big/ \left(\frac{3}{2\pi p_T^p}\frac{d^2N_p}{dydp_T^p}\right)^2 \tag{2.2}$$

where the $2\pi/3$ factor arises from the width of the three azimuthal regions. The experimental measurements are shown in Fig. 2.7 as a function of the transverse momentum per nucleon. The figure shows the measured coalescence parameter in and out of jets,

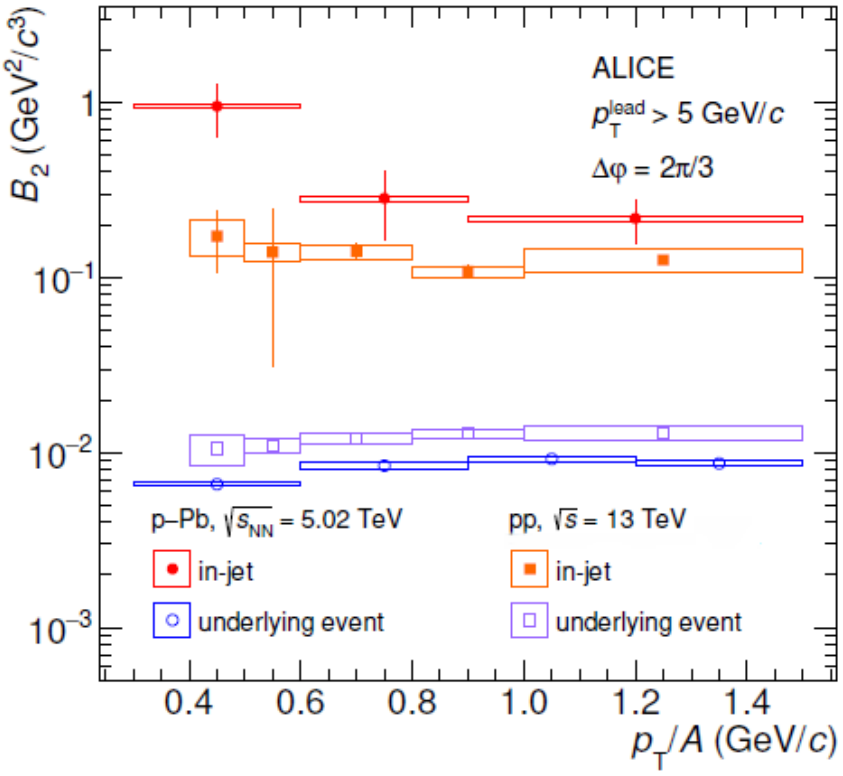


Figure 2.7: The coalescence parameter in jets and in the underlying event as a function of the per nucleon transverse momentum p_T/A (here, A = 2) in pp collisions at $\sqrt{s} = 13$ TeV [6] and p–Pb collisions at $\sqrt{s_{NN}} = 5.02$ TeV [20]. Jet-associated yields are obtained by subtraction between the Toward and Transverse regions, identified with respect to a leading track with $p_T > 5\,\mathrm{GeV/c}$. Statistical and systematic uncertainties are represented, respectively, by vertical bars and boxes. Modified from [20]

both in pp collisions at $\sqrt{s}$ = 13 TeV [6] (square markers) and in p–Pb collisions at $\sqrt{s_{NN}}$ = 5.02 TeV [20] (circle markers). In the latter case, the coalescence parameter in jets is enhanced with respect to that in the UE by more than a factor of 20, while an enhancement of about 15 is observed in pp collisions. The strong enhancement of B_2 in the jet-associated component provides evidence that deuteron formation is favoured in an environment with stronger nucleon correlations. Within coalescence models, this behaviour is consistent with a reduced effective phase-space separation of the nucleons. More information can be obtained if the values observed in the two collision systems are compared in the single azimuthal regions. In particular, in the underlying event region, the B_2 in p–Pb collisions is lower with respect to the same quantity in pp collisions. This is consistent with the dependence of the coalescence parameter on the source size. According to the coalescence model, the coalescence parameter decreases with increasing source size, since the nucleons are naturally more spread out in phase space. The source size of the pp and p–Pb colliding systems, in particular the values of the source radii, have been measured by ALICE through femtoscopy techniques. Typical values are of about 1 fm in pp collisions [12] and 1.5 fm in p–Pb collisions [7], actually depending on the pair transverse mass and on the event multiplicity. The different values of the coalescence parameter in jets, where the p–Pb values are larger than in pp collisions, do not have a unique explanation at the moment. They could arise from different hadrochemical composition of jets in the two systems (currently not expected), stronger momentum correlation between the nucleons, or possible differences in the leading-track kinematics. Moreover, a dependence on p_T/A is observed. In order to distinguish among these different explanations, specific analyses that investigate these hypotheses and a larger data sample might be considered, since the in-jet results are dominated by the statistical uncertainty.

2.2.2 Theoretical predictions on deuteron production in jets

The observed enhancement of deuteron production in jets has gained interest also from the theoretical point of view. We propose a simplified model from [48] to point out that actually two independent factors are responsible for the measured effect. The first one is a collimated emission of jet nucleons, and the second one is the smallness of a nucleon source, which is significantly smaller than a deuteron.

The yield of deuterons with momentum P can be written in the factorized form

$$\frac{dN_d}{d^3P} = \mathcal{A}\left(\frac{dN_p}{d^3\left(\frac{P}{2}\right)}\right)^2 \tag{2.3}$$

where we evaluated the proton momentum at half of the deuteron one, by assuming symmetry and uncorrelation between protons and neutrons. $\mathcal{A}$ is the deuteron formation rate, defined as

$$\mathcal{A} = \frac{3}{4}(2\pi)^3 \int d^3r H(\vec{r})|\varphi_d(\vec{r})|^2 \tag{2.4}$$

where $H(\vec{r})$ and $\varphi_d(\vec{r})$ are respectively the source function (in the center-of-mass frame of the deuteron) and the internal deuteron wavefunction described in chapter 3. The factor 3/4 reflects the fact that deuterons come from neutron-proton pairs in the spin triplet state, while a 1/2-isospin factor is absorbed in eq.(2.3). A specific feature of a jet is a strong collimation of jet particles around the leading one. To show how it influences deuteron production, we consider a highly simplified momentum distribution of jet nucleons. Setting the z axis along the trajectory of the leading particle, the yield of jet protons can be written as

$$\frac{dN_p}{d^3P} = N_p \frac{e^{-\alpha P}}{\pi\alpha^3} \frac{\Theta(\cos\theta - \cos\theta_c)}{1-\cos\theta_c} \tag{2.5}$$

where α is a real positive parameter, $\Theta(x)$ is the step function and θ_c is the critical polar angle such that jet nucleons are produced within the cone of angle θ_c. The angle expressed in radians approximately gives the so-called jet radius R, for mid-rapidity jets. The momentum distribution is normalized to N_p. Substituting this expression into Eq.(2.3) and integrating over the deuteron momentum, we get the total yield of jet deuterons

$$N_d^{jet} = \frac{2\mathcal{A}N_p^2}{\pi\alpha^3(1-\cos\theta_c)} \tag{2.6}$$

from which one can see that the deuteron yield grows when θ_c decreases, i.e. when the jet becomes more and more collimated.

Let us now discuss the role of the source function $H(\vec{r})$. Assuming a normalized-to-unity Gaussian parametrization for $H(\vec{r})$ and a Hulthén wavefunction for $\varphi_d(\vec{r})$, the formation rate $\mathcal{A}$ results in a monotonously decreasing function of r_0 with the maximum at $r_0 = 0$. The maximum value of $\mathcal{A}$ is reached when the radius of the nucleon source is much smaller than the deuteron radius, which is approximately 2 fm. Observing that the function $|\varphi_d(\vec{r})|^2$ changes slowly around $r = 0$, as compared to $H(\vec{r})$ when $r_0 \longrightarrow 0$, the value of $|\varphi_d(0)|^2$ can be pulled out of the integral in Eq.(2.4). Thus, one finds

$$\mathcal{A}^{\max} \simeq \frac{3}{4}(2\pi)^3 |\varphi_d(0)|^2 \tag{2.7}$$

which is independent of the adopted parametrization of the source function and it fully depends on the wavefunction at $r = 0$.

Comparing Eqs.(3.16) and (2.3), one finds that the coalescence parameter B_2 can be written as $B_2 = 2\mathcal{A}/m$, where m is the nucleon mass. The maximal value of B_2 corresponding to $\mathcal{A}^{\max}$ is $B_2^{\max} \simeq 0.33$ GeV^2/c^3. The experimentally found value of the coalescence parameter of jet deuterons in pp collisions at $\sqrt{s} = 13$ TeV is approximately $B_2 = 0.13 \pm 0.07$ GeV^2/c^3 [6], which is not far from the maximal value. Using the Hulthén wavefunction within this simplified model, effective source-size estimates of $r_0^{jet} = 0.3 \pm 0.2$ fm and $r_0^{UE} = 1.3 \pm 0.2$ fm are obtained [48]. These values are strongly model dependent, particularly because the jet-associated result probes the poorly constrained short-distance behaviour of the deuteron wave function.

Using a modern nucleon-nucleon potential like the Argonne v_{18}, which takes into account a hard-core repulsion at small distances, one finds that the deuteron wave function

is significantly reduced at $r \lesssim 1$ fm, when compared to the Hulthén wave function. Consequently, the deuteron formation rate from Eq.(2.7) is significantly reduced and it is too small to describe the deuteron production in jets. This problem reveals a fundamental incoherence: a potential such as Argonne is obtained from data on low-energy nucleon-nucleon scattering, but the deuteron wave function at small distances corresponds to relativistic momenta. The strong dependence on the short-distance wave function exposes a limitation of the simplified treatment. At such short distances, the separation between the source model and the nuclear wavefunction becomes resolution-dependent, and a more complete description may require additional short-range dynamics [48]. So, it is fair to say that the source of jet nucleons is much smaller than a deuteron and that the parameter r_0 is a fraction of 1 fm, but further quantification of this conclusion is rather uncertain. According to this conclusion, the whole process occurs at a length scale that is a fraction of a femtometer, which is however not surprising if one takes into account that jets are produced in hard scatterings with a momentum transfer of at least a few GeV/c and of the same scale of offshellness of the primarily produced partons. Consequently, the jet evolution occurs on a length scale of a fraction of a femtometer [48].

Experimentally, the jet-associated deuteron spectrum is harder than the underlying-event spectrum and its B_2 is strongly enhanced. These observations establish that the two event components provide distinct production environments. Their quantitative interpretation in terms of momentum collimation and source size remains model-dependent, motivating the differential study developed in the following chapters.

Chapter 3

Coalescence mechanism for (anti)nucleus formation

A fundamental question when approaching the study of antimatter bound states is how antinuclei, and more generally light nuclear clusters, form in high-energy reactions. High-energy collisions create a deconfined state of matter that resembles, in some ways, the state of matter of the early universe shortly after the Big Bang. When the hot and dense matter cools down, it forms hadrons and, occasionally, light nuclei and antinuclei. It is often argued that light nuclei, with a binding energy of a few MeV, are like "snowballs in hell", since the temperature of chemical freeze-out is about 155 MeV. The survival of light nuclei in such a hostile environment is a puzzle. Two broad phenomenological approaches are commonly used to describe light-nucleus yields. Statistical hadronisation models (SHMs) predict the abundances at chemical freeze-out from equilibrium statistical weights, without specifying the microscopic formation mechanism. Coalescence models instead describe nucleus formation in terms of the overlap in phase space between the constituent nucleons and the nuclear wave function.

Models of coalescence, have been used to describe microscopically the formation of composite objects as light nuclei and antinuclei for about sixty years. By coalescence, a nucleus is formed when nucleons are close enough in configuration and momentum space. Starting from the first model by Butler and Pearson in 1963 [33], coalescence evolved by introducing the density matrix formalism to calculate the nucleus formation probability, given by the integral over coordinate space of the projection of the proton and neutron wavefunctions over the deuteron one [55]. Following works drew attention to the constraint in coordinate space to be considered in heavy-ion collisions, where the source is a spatially-extended and collectively-expanding system. It has been pointed out that the source can be identified with the volume out of which particles are emitted with similar momenta, the size of which can be extracted by measuring two-particle momentum correlations with femtoscopy techniques [44]. It has been shown that the coalescence process depends on the size of the hadron emission region; more specifically, the relevant length scale for the process is the size of the nucleus relative to the size of the source [28]. Motivated by the need to model the production of light antinuclei in cosmic ray interactions for the estimate of

their flux near Earth, recent developments of the coalescence model focus on pp collisions, where small particle sources are expected. In particular, the work by Kachelriess et al. [43] provides a solution to apply coalescence as an afterburner to particle production.

In this study, we use a coalescence afterburner that takes into account realistic particle emission and correlations, to be used to simulate event-by-event (anti)deuteron production in high-energy hadronic collisions. The next section is devoted to showing the afterburner implementation [46], based on a state-of-the-art Wigner-function approach.

3.1 Wigner formalism

In order to properly formulate a coalescence model, we need to consider that coalescence is a quantum mechanical process. In this way, the classical definition of phase space is replaced by a description based on the Wigner formalism. In particular, our model adopts the procedure described in [29][46].

The relativistic single-particle Wigner function is defined as:

$$W(x,p) = \int d^4y\, e^{ip\cdot y}\, \psi^*\left(x - \frac{y}{2}\right) \psi\left(x + \frac{y}{2}\right) \tag{3.1}$$

where x and p are the 4-dimensional position and momentum and ψ is the single-particle field. The Wigner function can be used to extract the probability that a deuteron exists with a specific relative momentum and separation between its constituents.

In the process of deuteron formation via coalescence, the interactions of the nucleons of the pair with the rest of the particles are assumed to be subdominant due to the low particle density. The Lorentz-invariant yield of deuterons can be determined by projecting the deuteron density matrix ρ_d onto the two-nucleon density matrix ρ_{np}:

$$\gamma \frac{dN_d}{d^3P} = \mathrm{Tr}(\rho_d \rho_{np}) \tag{3.2}$$

Here, ρ_d represents the state $|\Psi_d\rangle\langle\Psi_d|$ with Ψ the (relativistic) momentum-dependent Bethe-Salpeter amplitude for bound states, while ρ_{np} accounts for the two-nucleon state $|\psi_p\psi_n\rangle\langle\psi_n\psi_p|$. By evaluating the trace in the above expression, one obtains

$$\gamma \frac{dN_d}{d^3P} = \frac{S}{(2\pi)^4} \int d^4x_1 \int d^4x_2 \int d^4x_1' \int d^4x_2'\, \Psi_d^*(x_1', x_2') \Psi_d(x_1, x_2) \rho_{np}(x_1, x_2; x_1', x_2') \tag{3.3}$$

where $S = 3/8$ is a factor that accounts for spin and isospin degeneracy. Also recall the fundamental relation:

$$\rho_{np}(x_1, x_2; x_1', x_2') = \langle x_1' x_2' |\, \rho_{np}\, | x_1 x_2 \rangle = \langle \psi_n^\dagger(x_2') \psi_p^\dagger(x_1') \psi_p(x_1) \psi_n(x_2) \rangle \tag{3.4}$$

We assume that the two-nucleon density matrix can be factorized into single-nucleon densities, which can be written in terms of the single-particle Wigner function as

$$\rho(x, x') = \int \frac{d^4p}{(2\pi)^4} e^{ip(x'-x)} W\left(\frac{x+x'}{2}, p\right) \tag{3.5}$$

from which we can infer the proton and neutron coordinates, $r_p = (x_1 + x_1')/2$ and $r_n = (x_2 + x_2')/2$ respectively. Moreover, the deuteron amplitude can be written factoring out the motion of the centre of mass:

$$\Psi_d(x_1, x_2) = e^{-iP\cdot R}\varphi_d(r) \tag{3.6}$$

where $R = (x_1 + x_2)/2$ is the space-time position of the deuteron, P its four-momentum, and $\varphi_d(r)$ is the internal spatio-temporal wavefunction, with $r = x_1 - x_2$ the relative position. Inserting Eqs.(3.5)(3.6) into Eq.(3.3) and rewriting the integral in terms of r, R (and the corresponding primed) variables, we get

$$\gamma\frac{dN_d}{d^3P} = \frac{S}{(2\pi)^4}\int d^4R \int d^4r \int \frac{d^4q}{(2\pi)^4}\,\mathcal{D}(r,q)\,W\left(R + \frac{r}{2}, \frac{P}{2} + q\right) W\left(R - \frac{r}{2}, \frac{P}{2} - q\right) \tag{3.7}$$

where q is the relative momentum between deuteron nucleons and $\mathcal{D}(r,q)$ is the relativistic Wigner function of $\varphi(r)$. Using the smoothness and equal-time approximations, as described in [29], in the pair rest frame (PRF) we obtain $P = (M, \vec{0})$, $q = (0, \vec{q})$ and the Bethe-Salpeter amplitude becomes independent of time in the non-relativistic limit. The time of *kinetic freeze-out*, $R^0 = t_{kf}$, represents the moment in which the momentum of the final-state particles is fixed. Assuming that t_{kf} is fixed and is the same for all particles, and considering that the particle yield is fixed at the common time of the chemical freeze-out, the integral over t_{kf} can be omitted. In addition, due to the time equalisation in the PRF, one can arbitrarily choose $t = r^0 = 0$. Hence, Eq.(3.7) reduces to a genuine three-dimensional equation:

$$\gamma\frac{dN_d}{d^3P} = \frac{S}{(2\pi)^6}\int d^3R \int d^3r \int d^3q\,\mathcal{D}(\vec{r},\vec{q})\,W_{np}\left(\vec{R},\vec{r},\vec{P},\vec{q}\right) \tag{3.8}$$

where we grouped the single-particle Wigner functions into the two-body object W_{np}. Notably, the starting point in this theoretical derivation is the single free nucleon momentum distributions and the deuteron wavefunction. We now make a semi-classical approximation where we assume a factorisation of space and momentum dependence of the proton–neutron Wigner function:

$$W_{np} = H_{np}(\vec{R},\vec{r};r_0)\,G_{np}(\vec{P}/2 + \vec{q}, \vec{P}/2 - \vec{q}) \tag{3.9}$$

where G_{np} is the two-particle momentum distribution, taken from Monte Carlo generators, containing the nucleon single-particle momentum distributions and final-state momentum correlations between the proton and neutron, including correlations induced by hadronisation and resonance decays; r_0 is the size of the two-particle emitting source. Finally, the coalescence probability can be written as the folding of the nucleon spatial distribution with the deuteron Wigner function:

$$\mathcal{P}(r_0, q) = \int d^3R \int d^3r\,H_{np}(\vec{R},\vec{r};r_0)\,\mathcal{D}(\vec{r},\vec{q}) \tag{3.10}$$

yielding the final form of the deuteron spectrum

$$\frac{dN_d}{d^3P} = \frac{S}{(2\pi)^6} \int d^3q\, \mathcal{P}(r_0, q)\, G_{np}(\vec{P}/2 + \vec{q}, \vec{P}/2 - \vec{q}) \tag{3.11}$$

For what concerns the space term H_{np}, spatial correlations are neglected so that it results as the product of the two single-particle distributions, which are assumed to be Gaussian. Finally we get

$$H_{np}(\vec{R}, \vec{r}; r_0) = \frac{1}{(2\pi r_0^2)^3} \exp\left(-\frac{r^2 + 4R^2}{4r_0^2}\right) \tag{3.12}$$

For a Gaussian source, the size of the two-particle emitting source (r_0) is related to the mean value (r_μ) of the two-particle distance distribution through $r_0 = (\sqrt{\pi}/4)r_\mu$. However, in particle generators the source has a shape that is generally not Gaussian [14]. For this reason, we evaluate r_μ from a fit to the distribution and then we obtain the source size r_0 through their relation.

Under the assumption of a Gaussian form also for the deuteron amplitude, saying

$$\varphi_d(r) = \frac{1}{(\pi r_d^2)^{3/4}} \exp\left(-\frac{r^2}{2r_d^2}\right) \tag{3.13}$$

We can analytically compute the Wigner distribution:

$$\mathcal{D}(\vec{r}, \vec{q}) = 8e^{-q^2 r_d^2}\, e^{-r^2/r_d^2} \tag{3.14}$$

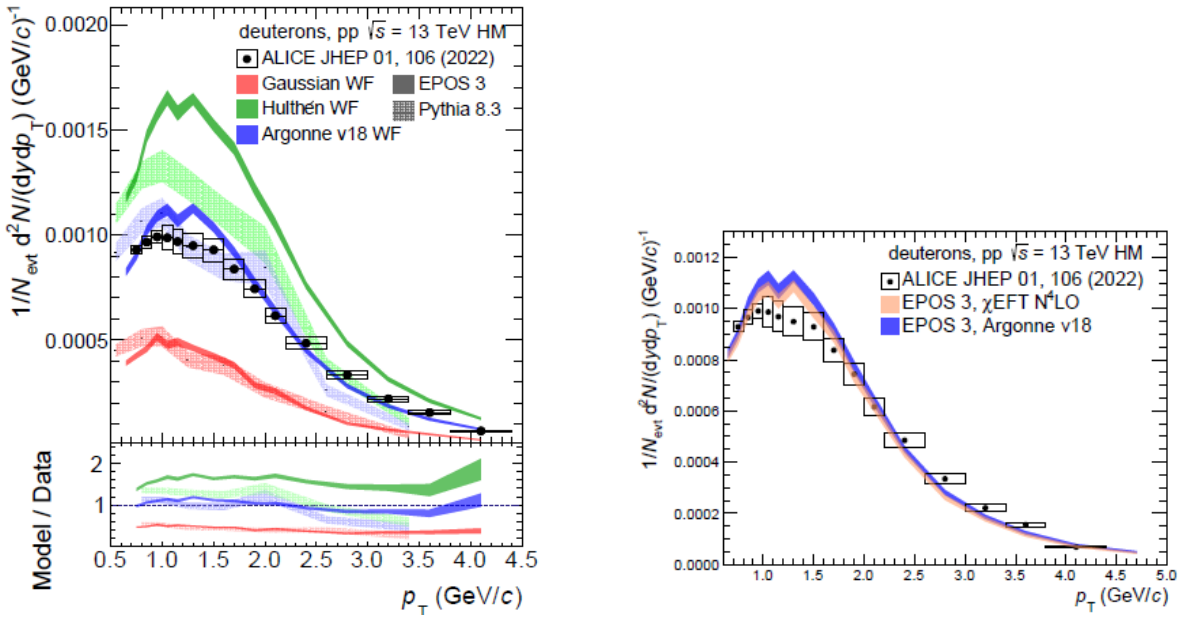
where $r_d = 3.2$ fm is the characteristic size parameter of the deuteron wavefunction (corresponding to an RMS charge radius of about 2.1 fm). In this case, we get the coalescence weight

$$\mathcal{P}(r_0, q) = \eta 8 e^{-q^2 r_d^2} \tag{3.15}$$

with $\eta = \left(\frac{r_d^2}{r_0^2 + r_d^2}\right)^{3/2}$. Formally, this is not a probability, as $\mathcal{P}(r_0,\, \mathrm{q}) \in [0,\, 8]$. This is due to the definition of the Wigner function.

3.2 Test of the deuteron wavefunction

The Wigner function formalism described in the previous section is employed to obtain the deuteron spectra starting from nucleons simulated with Monte Carlo generators. At midrapidity and LHC energies, the neutron spectrum is commonly approximated by the measured proton spectrum, relying on approximate isospin symmetry and the dominance of pair production. Spectra are reweighted to match the proton measurement by ALICE [13] and start from realistic transverse momentum distributions. For each generated event, the coalescence probability $\mathcal{P}(r_0, q)$ for the single proton-neutron pair, which also depends on the deuteron wavefunction $\varphi_d(r)$.



(a) (b)

Figure 3.1: Deuteron spectra obtained from MC generators in high-multiplicity pp collisions at $\sqrt{s} = 13\,\text{TeV}$, applying the coalescence model with different hypotheses for the deuteron wavefunction, compared with the ALICE measurement [13]. The width of the bands represents the statistical uncertainty of the models. a) includes data-to-model ratios, in the bottom panel. b) compares Argonne v_{18} and χEFT as wavefunction hypotheses. From [46]

Three different wavefunctions are considered: a Gaussian, Hulthén [42], and Argonne v_{18} [65]. Whereas the Gaussian is the simplest functional form of the wavefunction, the Hulthén and Argonne v_{18} are based on physical properties of the deuteron. The Argonne v_{18} wave function is obtained from a high-precision nucleon-nucleon potential fitted to scattering data, whereas the Gaussian and Hulthén forms provide simpler reference parametrisations. The shape of the deuteron wavefunction in the asymptotic region ($r \gtrsim 1.5$ fm) is determined by the solution of the Schrödinger equation for an interaction potential that reproduces the deuteron binding energy correctly. In this range, Hulthén and Argonne v_{18} are very similar. In the range $r \lesssim 1.5$ fm, the two wavefunctions drastically differ, as a consequence of the different p-n potentials. Indeed, the Hulthén potential does not include the short-range suppression due to the repulsive core of realistic potential, while the Argonne v_{18} does. A difference in the predicted yields computed with the two wavefunctions suggests that the nuclear production mechanism is sensitive to the short-range strong interaction between nucleons. Figure 3.1a shows the deuteron spectra obtained with the different wavefunctions and different event generators. The results using the Argonne v_{18} wavefunction are in excellent agreement with the data measured by ALICE, regardless of the event generator used. Within the assumptions of the model and after constraining the nucleon spectra, charged-particle multiplicity and source size, the calculation using the

Argonne v_{18} wavefunction provides a good description of the measured deuteron spectrum. This agreement supports the relevance of a realistic treatment of the nuclear wave function, although it does not yet establish a unique microscopic description.

In order to further test the impact of the core part of the strong-interaction potential on the deuteron yield, the deuteron wavefunction obtained from *ab initio* Chiral Effective Field Theory (χEFT) (N^{4}LO) calculations [39] are employed to compute the deuteron yield [46] and the results are compared with those obtained using the Argonne v_{18} wavefunction (see Fig. 3.1b). The χEFT potential is derived systematically from the underlying theory of QCD and involves a perturbative expansion in powers of a small parameter related to the pion mass. While Argonne v_{18} and χEFT are two different approaches, the deuteron wavefunctions obtained from these approaches do not differ significantly, except for very short ranges. Indeed, the deuteron wavefunction from χEFT shows less repulsion than the one obtained from the Argonne v_{18} potential. Nevertheless, the predicted deuteron yields using Argonne v_{18} and χEFT are compatible, indicating that, within the model precision, differences between these two wavefunctions at short distances don't produce a visible effect.

3.3 Coalescence parameter

The relation between the deuteron spectrum and the initial proton and neutron momentum distributions is described by the so-called *coalescence parameter* B_A. We take the momentum distribution of a (anti)nucleus with mass number A as the product of the momentum distributions of the protons and neutrons that constitute the nucleus, multiplied by the probability B_A that the process occurs. Since neutrons are typically difficult to detect experimentally, we assume their energy distribution to be equal to that of protons, yielding

$$E_A \frac{dN_d}{d^3P} = B_A \left(E_p \frac{dN_p}{d^3p_p} \right)^A \Bigg|_{p_p = P/A} \tag{3.16}$$

In a simple coalescence approach [33], B_A is expected to be independent of momentum and of the object size relative to the volume of particle emission, namely the source size. While this picture is found to be approximately valid in pp and p-Pb collisions, it breaks down in Pb-Pb collisions, which exhibit a strong decrease in B_A with centrality, i.e. the degree of overlap between colliding nuclei. We have seen that a full quantum mechanical treatment of coalescence takes into account the source size, as the coalescence probability naturally decreases for nucleons with similar momenta that are produced far apart in configuration space.

In this model, the coalescence parameter B_2 is computed using the deuteron and proton invariant spectra in the transverse momentum, so that

$$B_2 = \left(\frac{1}{2\pi P_T} \frac{d^2N_d}{dy dP_T} \right) \Bigg/ \left(\frac{1}{2\pi p_T^p} \frac{d^2N_p}{dy dp_T^p} \right)^2 \tag{3.17}$$

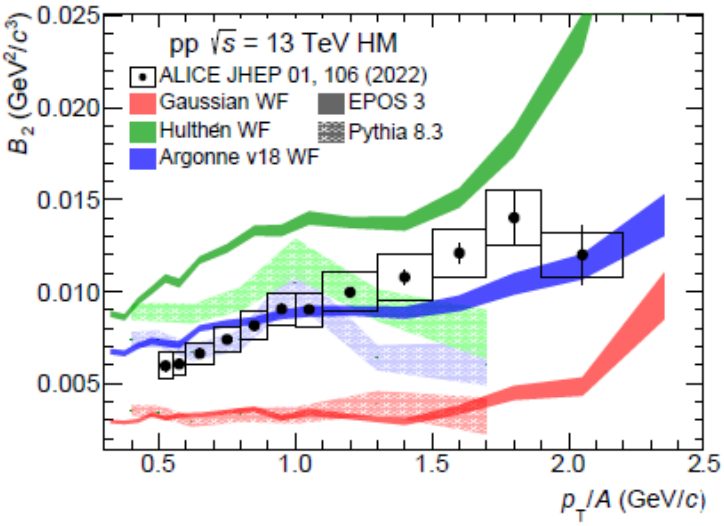


Figure 3.2: Coalescence parameter B_2 obtained with EPOS 3 and Pythia 8.3, compared with the ALICE measurement [13]. From [46]

where the proton transverse momentum is taken as half of the deuteron one ($p_T^p = P_T/2$) and both protons and deuterons are identified at midrapidity. The comparison among the B_2 measured by ALICE [28] and those obtained using MC generators [46] is shown in Fig.3.2. The better agreement with experimental data is again achieved by using the Argonne v_{18} wavefunction for the deuteron. The predictions using a Gaussian wavefunction underestimate the coalescence parameter by about 50 to 70%, while the predictions using the Hulthéen wavefunction overestimate the measured B_2 by about 20 to 50%.

The Wigner-function approach therefore identifies two ingredients that are central to the work carried out in this thesis: the momentum correlations of the nucleons and the size of their effective emission region. Jet-associated production and the underlying event provide markedly different environments in which these ingredients, and consequently B_2, can be investigated.

3.4 Alternative modeling of nucleus production

An alternative approach to study and predict nucleus production is to statistically assess the abundances of different particle species produced in particle collisions. Statistical hadronisation models (SHMs) [27] predict the production of light hadrons and nuclei as a function of temperature, volume, and baryochemical potential starting from the partition function of a non-interacting quantum gas of hadrons and resonances in chemical equilibrium. The temperature determines the average kinetic energy of particles and influences the probability of forming heavier states such as nuclei, depending on their mass. The

chemical potentials enforce the average conserved charges of the system; at LHC energies, the baryochemical potential at midrapidity is close to zero. The SHM assumes that nuclei are formed at the so-called *chemical freeze-out*, which is the stage of the system expansion when the abundances of particles are fixed under equilibrium conditions. SHMs are successful in describing the production yields of light (anti)nuclei together with other light hadrons in central heavy-ion collisions from Relativistic Heavy Ion Collider to the LHC, where up to a few tens of thousands of particles are produced (hence justifying a statistical approach). However, the SHM does not provide a microscopic model of nucleosynthesis and is agnostic of the binding energy and wavefunction of the nucleus.

As we have seen, pp collisions produce a small reaction volume so that the hadron-resonance gas resulting from the interaction can be described using a canonical ensemble. In this case, we must impose local charge conservation. In particular, the electric charge, the strangeness and baryon number are set to fixed values and exactly conserved within the volume. This leads to the so-called canonical suppression for particles carrying the conserved charges. This is mostly relevant for strange particles, since the large masses and the small available volume disfavour the production of both hadrons carrying opposite strangeness.

Chapter 4

Simulation tools

In this chapter, we introduce the simulation tools used in the analysis. Proton-proton events are generated with `PYTHIA 8.3` [30], jets are reconstructed with `FastJet` [35] using the anti-k_t algorithm [34], and deuteron production is modelled by applying a coalescence afterburner to the generated proton-neutron pairs [46]. Whereas the focus in this chapter is on the general principles of the simulation tools, the complete generator configuration, jet-definition parameters and event selections adopted for the analysis are reported in chapter 5.

4.1 `PYTHIA 8.3` event generation

`PYTHIA` [30] is a scientific code library that is widely used for the Monte Carlo generation of events in high-energy collisions between elementary particles in various combinations, including heavy-ion collisions. The package contains theory and models for a number of physical aspects, including total and partial cross sections, hard and soft interactions, parton distributions, initial- and final-state parton showers, matching and merging of matrix elements and showers, multiparton interactions, hadronization, fragmentation and decays. `PYTHIA 8.3` incorporates a comprehensive set of tools to model particle interactions, particularly focusing on the strong interaction, described by quantum chromodynamics (QCD), and phenomena extending beyond the Standard Model (BSM). The tool can also simulate specific processes which are relevant for astrophysical events, such as dark matter annihilation into Standard Model particles, particle showers, or hadronization.

At a basic level, an event consists of a number of outgoing particles that might be recorded in a snapshot taken by an idealized detector, with conservation laws constraining the values of total energy and momentum or any other conserved quantum number. A numerical algorithm that can produce random sequences of simulated events is called an *event generator*. A high-energy physics event is a list of the subatomic particles produced in a collision, namely the *event record*. In `PYTHIA` it includes the four-momentum, status code and many other properties of each particle. One can also require to keep trace of the production point, which is different from the origin for decay products. Typically,

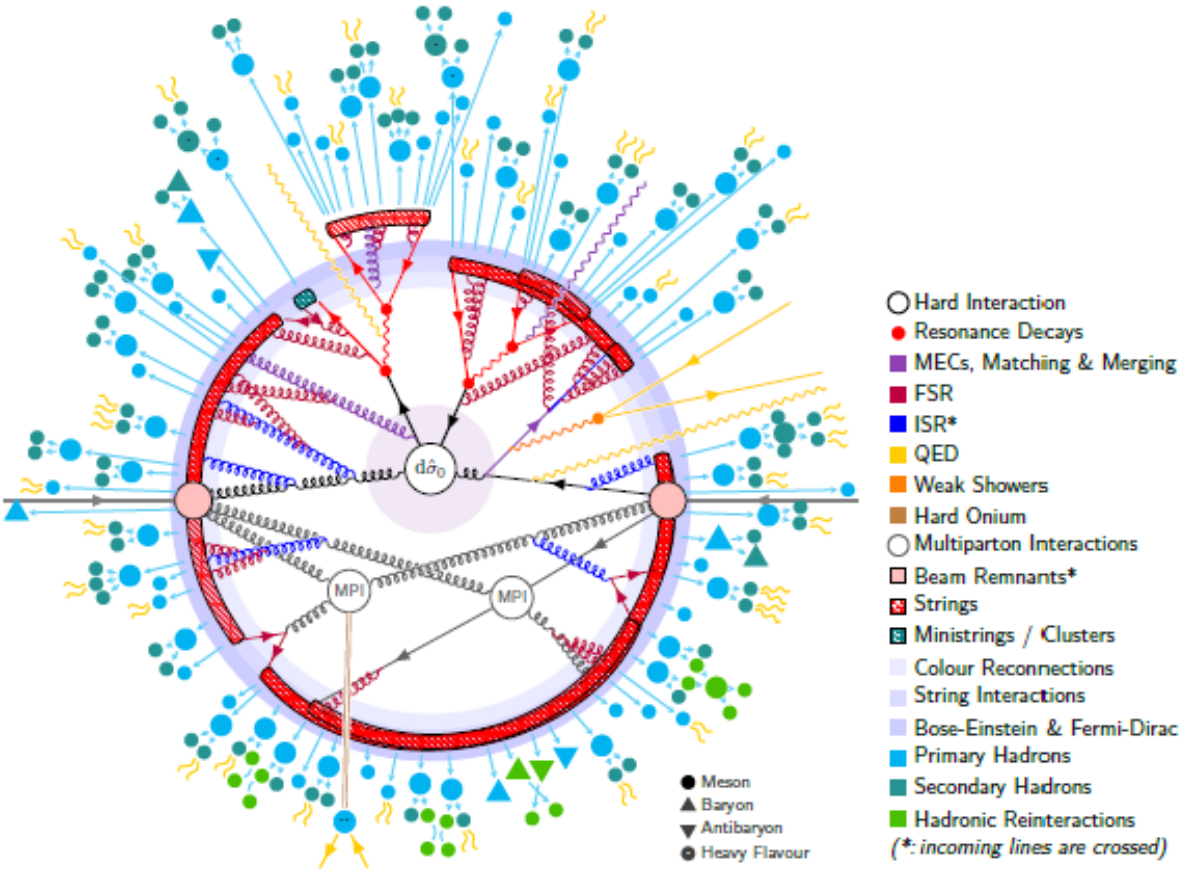


Figure 4.1: Diagrammatic and simplified structure of a PYTHIA event. From [30]

the event record also includes the history of a particle, keeping trace of its decay chain (*mother-daughter* relationship). Depending on the generation mode, events may also carry weights, while PYTHIA reports the cross section associated with the generated process sample.

The full properties of an event, however, cannot currently be calculated from first principles alone. Many different, complex phenomena, which are likely related, are described by phenomenological models or parametrizations that each apply on a limited dynamical range. As a result, the predictions of an event generator like PYTHIA 8.3 depend upon $\mathcal{O}(100)$ parameters. A collection of such parameter values is referred to as a *tune*. The default tune, Monash 2013 [58], was calibrated on the basis of Tevatron and LHC data.

PYTHIA event generation is structured into three main levels:

- **Hard process:** initial stage, which handles the main scattering process.
- **Parton shower:** initial and final-state radiation, including soft-gluon emissions and collinear parton splittings.

- **Hadronization:** non-perturbative stage where partons combine into colorless hadrons, following string fragmentation.

Several physical processes can be handled by `PYTHIA`:

- **QCD processes:** hard and soft QCD interactions, with an accurate treatment of light and heavy quarks, as well as gluon interactions.
- **Electroweak processes:** production of photons, W/Z bosons, and other electroweak particles.
- **Beyond-Standard-Model processes:** `PYTHIA` can also deal with supersymmetry, dark matter annihilation and other BSM effects.

4.1.1 Lund String Model

The Lund String Model [22] is a widely used theoretical framework in `PYTHIA` for describing the hadronization process. The model is based on the QCD principle of confinement, i.e. the fact that quarks cannot exist as free particles but must always be bound into hadrons, due to the increasing strength of the strong interaction as they move apart. In the Lund String Model, quarks and gluons are connected by a one-dimensional *string* of colour field, Fig.4.2. When two quarks are pulled apart in a collision, this string stretches. At sufficiently large separations, the potential energy of a colour-connected quark-antiquark system increases approximately linearly with distance, corresponding to an approximately constant string tension. When the stored energy becomes large enough, the string can break through the production of a new quark-antiquark pair from the vacuum, resulting in two smaller string systems. These quarks combine together until colourless hadrons are formed and no colour string is left. This is actually a probabilistic process, where the probability of string breaking and the resulting momentum distribution of the produced hadrons follow precise model-based rules. The Lund String Model also accounts for various important effects such as colour reconnection [36], where the colour flow in a collision event can change due to interactions between different strings, and baryon production, which can occur via string junctions [23] or "popcorn" mechanism from diquark-antidiquark pairs [45]. More details on colour reconnection will be given in chapter 5, since these processes are activated in the tune chosen specifically for the work of this thesis.

In `PYTHIA`, the Lund String Model is implemented as the default hadronization mechanism for most processes involving quarks and gluons. It is responsible for simulating the transition from a high-energy parton-level interaction, where quarks and gluons are produced, to a final state where these partons are bound into hadrons that can be detected in experiments. One of the strengths of the Lund String Model is its ability to describe a wide range of phenomena in hadron-hadron, lepton-hadron, and even heavy-ion collisions. The model parameters, such as the string tension (the force per unit length along the string) and the probability for string breaking, can be adjusted to fit different experimental conditions, making it a versatile tool for studying particle physics.

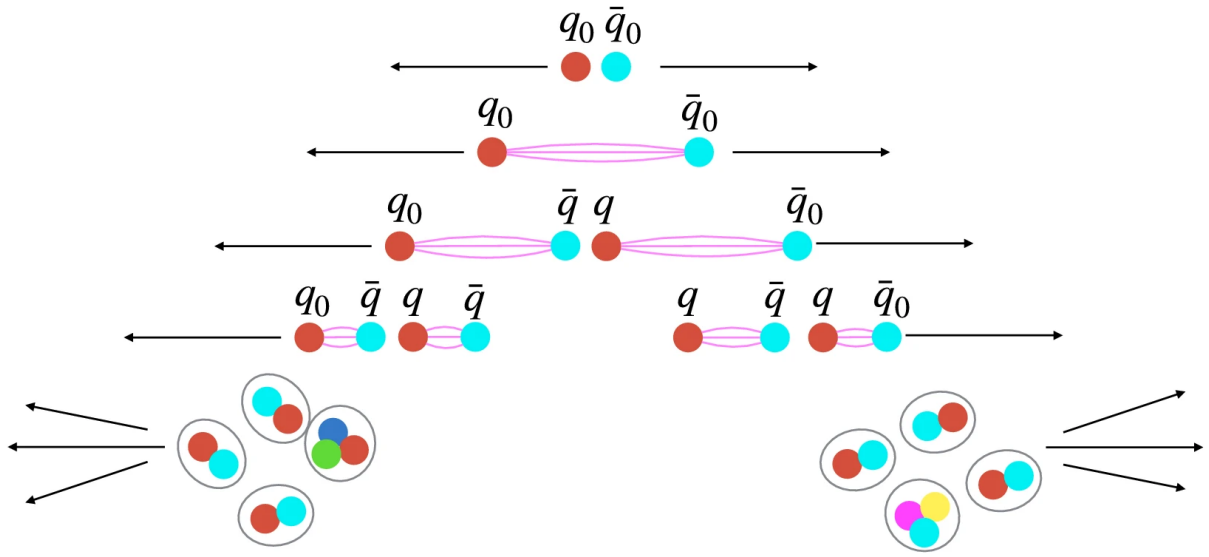


Figure 4.2: Schematic representation of the string fragmentation process. From [22]

In summary, the Lund String Model plays a crucial role in `PYTHIA` by providing a detailed and physically motivated description of the hadronization process. By modelling the confinement of quarks and the fragmentation of the color string, it allows `PYTHIA` to simulate realistic final states that closely match the particles observed in collider experiments.

4.2 Jet reconstruction with `FastJet`

`FastJet` [35] is a software package that provides a broad range of jet finding and analysis tools. It includes efficient native implementations of all widely used jet algorithms for pp and e^+e^- collisions, together with facilities to manipulate jet substructures, tools for determination of jet areas and subtraction or suppression of noise in jets.

Jets tend to be visually obvious structures when one looks at an experimental event display; however, their behaviour must be well defined and reproducible: one should have rules that project a set of particles onto a set of jets. Such a set of rules is a *jet algorithm*: it defines a jet on the basis of one or more parameters that govern its detailed behaviour. A suitable jet algorithm should be infrared and collinear safe: the reconstructed jets must remain unchanged when an arbitrarily soft particle is added or when one particle undergoes a collinear splitting.

It is possible to classify most jet algorithms into two broad classes [54]: sequential recombination algorithms and cone algorithms.

Sequential recombination algorithms usually identify the pair of particles that are closest in some distance measure, recombine them, and then repeat the procedure over and over again until some stopping criterion is reached. The various sequential recombination algorithms differ mainly in their particular choices of distance measure and stopping

criterion.

Cone algorithms put together particles within specific conical angular regions, notably such that the momentum sum of the particles contained in a given cone coincides with the cone axis (forming a *stable cone*). Because QCD radiation and hadronization leave the direction of a parton's energy flow essentially unchanged, the stable cones are physically close in direction and energy to the original partons. Differences between various cone algorithms are essentially given by the strategy employed to search for the stable cones and the procedure to deal with cases where the same particle is found in multiple stable cones.

Sequential recombination algorithms can be written down in a general form, usually called the k_t *algorithm*. It involves a (symmetric) distance measure (d_{ij}) between all pairs of particles i and j, as well as a beam distance (d_{iB}) for each particle:

$$d_{ij} = \min\left(k_{ti}^{2p}, k_{tj}^{2p}\right)\frac{\Delta_{ij}^2}{R^2}, \qquad d_{iB} = k_{ti}^{2p} \tag{4.1}$$

where k_t is the transverse momentum with respect to the beam (z) direction,
$\Delta_{ij}^2 = (y_i - y_j)^2 + (\phi_i - \phi_j)^2$ with y and ϕ respectively the rapidity and azimuthal angle and R, p are user-defined parameters. In the so-called *inclusive* formulation of the k_t algorithm, one identifies the smallest of the d_{ij} and d_{iB}. If it is a d_{ij}, traces i and j are replaced with a single new object whose momentum is $k_i + k_j$; this is called a *pseudojet*, since it is neither a particle, nor yet a full jet. If instead the smallest distance is a d_{iB}, then i is removed from the list of particles/pseudojets and added to the list of final jets. The clustering continues until no particles or pseudojets remain. Of the final jets, generally only those above some transverse momentum are actually used.

The R parameter is usually referred to as the jet radius and determines the characteristic angular extent of the jet in the $y - \phi$ space. The parameter p, instead, controls how the transverse momentum of the particles enters the distance measure and therefore determines the clustering order. In particular,

- $p = 1$ corresponds to the k_t algorithm, in which softer particles tend to be clustered first;
- $p = 0$ corresponds to the Cambridge/Aachen algorithm, for which the clustering is determined only by the angular separation;
- $p = -1$ corresponds to the anti-k_t algorithm, in which clustering proceeds preferentially around hard particles.

Thus, the sign of p determines whether the clustering is preferentially driven by soft or hard particles, while $p = 0$ removes the transverse-momentum dependence from the distance measure. The remaining of this section focuses in particular on the anti-k_t algorithm as it is the one employed for the work of this thesis.

A difficulty that arises in the implementation of a sequential-recombination jet finding algorithm is that at hadron colliders, clustering is often performed with several hundreds

or even thousands of particles. Given N particles, there are $N(N-1)/2$ d_{ij} distances to calculate, and since one must identify the smallest of these $\mathcal{O}(N^2)$ distances at each of $\mathcal{O}(N)$ iterations of the algorithm, original implementations involved $\mathcal{O}(N^3)$ operations to perform the clustering, which quickly becomes prohibitive given that it can be necessary to cluster hundreds of millions of events. To alleviate this problem, `FastJet` makes use of the observation that the smallest pairwise distance remains the same if one uses the following alternative (non-symmetric) distance measure:

$$d_{ij} = k_{ti}^{2p}\frac{\Delta_{ij}^2}{R^2}, \qquad d_{ji} = k_{tj}^{2p}\frac{\Delta_{ij}^2}{R^2}, \tag{4.2}$$

For a given i, the closest particle in this new distance measure is simply found by identifying the i's geometrical nearest neighbour on the y-ϕ cylinder. Geometry adds many constraints to closest pair and nearest neighbour type problems, e.g. if i and j are geometrically close to k, then i and j are also geometrically close to one another; such a property is not true for the original symmetric distance. The factorisation of the problem into momentum and geometrical parts makes it possible to calculate and search for minima among a much smaller set of distances. This is sufficiently powerful that with the help of the external Computational Geometry Algorithms Library, `FastJet` achieves expected $N \ln N$ timing for many sequential recombination algorithms.

4.2.1 Anti-k_t algorithm

The functionality of the anti-k_t algorithm [34] can be understood by considering an event with a few well-separated hard particles with transverse momenta $k_{t1}, k_{t2}, \ldots$ and many soft particles. The $d_{1i} = \min(1/k_{t1}^2, 1/k_{ti}^2)\,\Delta_{1i}^2/R^2$ between a hard particle 1 and a soft particle i is exclusively determined by the transverse momentum of the hard particle and the Δ_{1i} separation. The d_{ij} between similarly separated soft particles will instead be much larger. Therefore, soft particles will tend to cluster with hard ones long before they cluster among themselves. If a hard particle has no hard neighbours within a distance $2R$, then it will simply accumulate all the soft particles within a circle of radius R, resulting in a perfectly conical jet.

If another hard particle 2 is present such that $R < \Delta_{12} < 2R$, then there will be two hard jets. It is not possible for both to be perfectly conical. If $k_{t1} \gg k_{t2}$, then jet 1 will be conical and jet 2 will be partially conical, since it will miss the part overlapping with jet 1. For a general situation, $k_{t1} \sim k_{t2}$, both cones will be clipped, with the overlapping part divided between the two.

Similarly, one can work out what happens with $\Delta_{12} < R$. Here particles 1 and 2 will cluster to form a single jet. If $k_{t1} \gg k_{t2}$ then it will be a conical jet centred on k_1. For $k_{t1} \sim k_{t2}$ the shape will instead be more complex, being the union of cones (radius $< R$) around each hard particle plus a cone (of radius R) centred on the final jet.

The key feature above is that the soft particles do not modify the shape of the jet, while hard particles do. In other words, the jet boundary in this algorithm is resilient with respect to soft radiation, but flexible with respect to hard radiation.

The behaviours of different jet algorithms are illustrated in Fig.4.3. A parton-level event together with $\sim 10^4$ random soft 'ghost' particles is clustered with 4 different jet algorithms. For each of the partonic jets, we have shown the region within which the random ghosts are clustered into that jet. For the k_t and Cambridge/Aachen algorithms, that region depends somewhat on the specific set of ghosts, and the jagged borders of the jets are a consequence of the randomness of the ghosts - the jet algorithm is adaptive in its response to soft particles. For SISCone (a Seedless Infrared-Safe Cone jet algorithm) one sees that single-particle jets are regular, while composite jets have more varied shapes. Finally with the anti-k_t algorithm, the hard jets are all circular with a radius R, and only the softer jets have more complex shapes.

The specific jet definition used in this analysis, including the radius parameter, constituent selection, kinematic acceptance and jet-level requirements, is given in chapter 5.

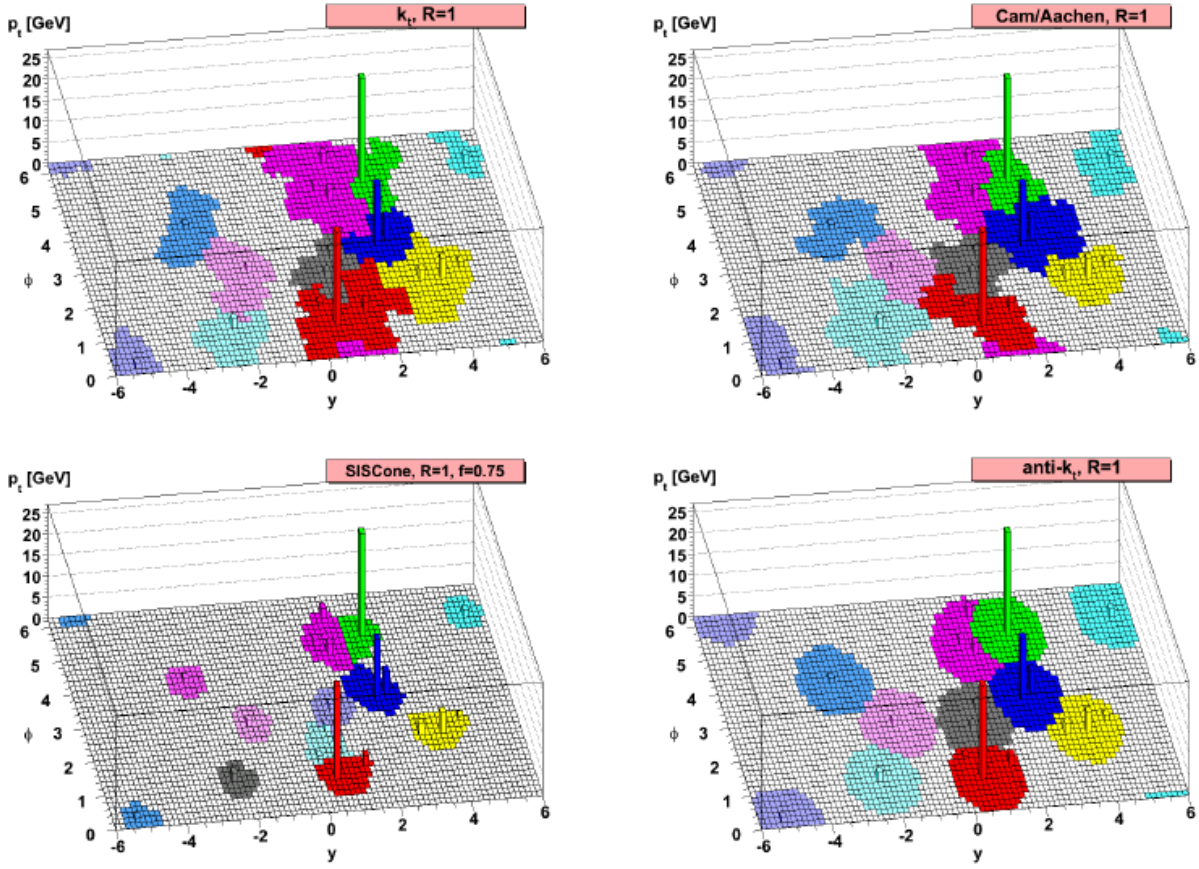


Figure 4.3: A sample parton-level event, together with many random soft "ghosts", clustered with four different jet algorithms, illustrating the areas of the resulting hard jets. For k_t and Cam/Aachen, the detailed shapes are in part determined by the specific set of ghosts used. From [35]

4.3 Coalescence afterburner

Deuteron formation is simulated by means of the coalescence afterburner developed in [46], applied to the hadronic final state generated by `PYTHIA`. The code implements the Wigner-function formalism introduced in chapter 3. Within this thesis, selected aspects of the algorithm were tested and specific options relevant to jet-associated production were implemented or validated, as detailed in chapter 5.

The code reads in input, for each event, the list of outgoing particles, together with their kinematic information, such as momentum, rapidity, production position and time, mother particle.

Nucleons are selected and classified into two categories: *prompt*, if they are produced in the hadronization stage and do not come from a resonance decay, or *resonance feeddown* if they originate from a resonance decay. The two populations, separately for protons and neutrons, are stored in distinct arrays. When requested at generation level, `PYTHIA` also provides the production vertices and times of the particles in the event record. This information is used by the afterburner to reconstruct the relative space-time separation of each proton–neutron pair. For feeddown nucleons, the decay vector, i.e. the difference between the decay point and the resonance production point, is also computed. The afterburner also provides an optional reweighting of the primordial and resonance-feeddown components based on statistical-hadronisation estimates [64]. `PYTHIA` may indeed underestimate the fraction of feeddwon and moreover, it implements only Δ resonances while other (heavier) excited nucleon states are not present. This tuning option was introduced for inclusive particle production and used, for instance, in [46]. Its applicability to jet fragmentation, however, is not established, since the assumptions of a partially equilibrated source and a finite correlation volume need not hold inside jets. The choice adopted in this analysis is therefore specified in chapter 5.

The coalescence probability depends also on the spatial extension of the source from which the two nucleons are emitted, which is modelled as a Gaussian of width σ. Three ways of determining σ are currently implemented in the aferburner: a fixed value to be set as an input parameter, a functional parametrization of the pair transverse mass tuned to ALICE data [15] or the event-by-event native value derived from `PYTHIA` positions and times. This last value also accounts for the spatial offset introduced by resonance feeddown nucleons and is rescaled by a factor $4/\sqrt{\pi}$ to convert it into an equivalent Gaussian sigma.

The core of the algorithm consists of four double loops (one for each p-n combination: prompt-prompt, prompt-resonance, resonance-prompt, resonance-resonance), which run over all proton-neutron pairs in the event. For each candidate pair, the total four-momentum $P = p_p + p_n$ is computed in the laboratory frame. The pair rest frame (PRF) is reached by a Lorentz boost with velocity $\vec{\beta} = \vec{P}/E$. The four-momenta and four-position vectors of both nucleons are transformed to this frame, giving $p^*_{p,n}$ and $r^*_{p,n}$. Also, the two particles are brought to a common time by freely propagating the earlier-emitted nucleon to the emission time of the later one. Two quantities can then be built at this equal time:

$$k^* = \frac{1}{2}\left|\vec{p}_p^{\,*} - \vec{p}_n^{\,*}\right|, \qquad \Delta R = \left|\vec{r}_p^{\,*} - \vec{r}_n^{\,*}\right|, \tag{4.3}$$

where k^* is the relative momentum and ΔR is the spatial separation of the two nucleons in the PRF. Pairs with k^* above a fixed threshold are discarded before the probability is computed, since the deuteron wave function gives a negligible contribution there.

The actual coalescence condition is evaluated by comparing the pair relative momentum and relative distance against the selected deuteron internal wave function. The main choices available for the deuteron wavefunction are mentioned in section 3.2. Pairs satisfying the condition are considered formed deuterons and are histogrammed separately for each of the four formation channels (in both transverse momentum (p_T) and rapidity spectra), applying as a weight the product of the prompt/feeddown factors, if enabled, and the deuteron spin-isospin statistical factor equal to 3/8. Finally, the afterburner provides as output the transverse momentum (p_T) distribution of deuterons as the sum of the four formation channels. A rapidity selection and normalization to a specific event class were applied as specific choices of the analysis. As default, the normalization is to the INEL > 0 event class collecting all inelastic events with at least one charged particle in the central rapidity region, specifically introduced to allow for comparison with ALICE data. The generator settings, wavefunctions, phase-space selections, treatment of competing pairs, jet association and spectrum normalisation adopted in this thesis are presented together in chapter 5.

Chapter 5

Study of deuteron production

We have already discussed (see chapter 2) the importance of collecting data on (anti)deuteron production in high-energy collisions, in order to improve models and predictions for cosmic antideuteron fluxes and the related astrophysical background. Data from accelerator-based experiments such as ALICE also suggest that the coalescence mechanism is able to provide a microscopic description of nucleus formation. Since in this model nuclei come from nucleons close in phase space, it is convenient to analyse their production in jets, where the phase-space proximity is naturally implemented. Experimental measurements have been carried out by ALICE and are reported in subsection 2.2.1. This work aims to establish and benchmark a simulation chain that exploits PYTHIA and a coalescence-based approach to be used to predict (anti)deuteron production for comparison with available and future ALICE data (see chapter 4).

In this chapter, we discuss our own configuration for the simulation tools presented earlier, and we introduce our analysis of jet kinematics and the study of in- and out-of-jet deuteron production. We present data for deuterons but the same results hold for antideuterons. Indeed, we have verified that the production of nucleons and antinucleons is symmetric in the generator at the studied energy, and moreover, under the assumption of the validity of the CPT theorem, coalescence applies in the same way for matter and antimatter.

5.1 Configuration of simulation tools

In this section, we introduce our own configuration options and parameters for the simulation tools. In particular, we specify the `PYTHIA` tune, the `FastJet` parameters and event selection, the coalescence afterburner settings and the count of coalescing pairs.

5.1.1 `PYTHIA` tune and `FastJet` configuration

Proton-proton collisions at $\sqrt{s} = 13.6\,\text{TeV}$, corresponding to the LHC Run 3 centre-of-mass energy, were simulated using `PYTHIA 8.3`. Inelastic events were generated by enabling all

soft QCD processes, while hard and low-energy QCD processes were explicitly switched off; this choice ensures that the full inelastic cross section is sampled, rather than only final states arising from hard parton scatterings.

The `PYTHIA` tune chosen for this study is the so-called *Tune 2M*, introduced by [37] and predating the Monash 2013 tune [58] (which is the current `PYTHIA 8.3` default). It constrains the parameters governing initial-state radiation, multi-parton interactions (MPI) and beam remnants, i.e. the aspects of the event most sensitive to non-perturbative QCD in hadronic collisions, using the Martin–Roberts–Stirling–Thorne leading-order parton distribution functions [57]. Since each tune fixes an internal set of default parameters, any subsequent command in the configuration file overrides the corresponding tune value; in this configuration, all colour-reconnection-related settings are indeed specified explicitly afterwards, superseding whatever colour-reconnection behaviour is associated with Tune 2M by default. The colour reconnection mode allows the interaction and merging of different colour strings, in favour of minimal energy configurations. In our specific mode, coloured strings are treated according to an SU(3)-inspired algebra, allowing reconnections that minimise the total string length across the whole event. Colour reconnection is restricted to strings that are in causal contact: if a boosted string has already decayed (hadronised) before another one has even formed, no reconnection between them is allowed, since no space-time region exists where the two colour charges could physically interact. This mechanism suppresses reconnections between causally disconnected partons, and is the feature that allows the model to reproduce collective, radial-flow-like effects observed in high-multiplicity pp collisions at the LHC [11] without invoking an explicit hydrodynamic description. This is the reson why we chose to include colour reconnection in our tune.

Hadronisation proceeds via the Lund string fragmentation model. The longitudinal momentum sharing between the produced hadrons is governed by the Lund symmetric fragmentation function, with parameters `StringZ:aLund = 0.36` and `StringZ:bLund = 0.56`, while the transverse-momentum kick at each string breakup follows a Gaussian distribution of width `StringPT:sigma = 0.335 GeV/c`.
Baryon production proceeds through diquark-antidiquark pair creation at string breaks, with relative probability `StringFlav:probQQtoQ = 0.078` with respect to quark-antiquark pair creation, and the relative probabilities of spin-1 diquark states are set via `StringFlav:probQQ1toQQ0join`. Strangeness suppression at the string level, distinct from the canonical suppression discussed in the statistical hadronisation picture (section 3.4), is controlled by `StringFlav:ProbStoUD=0.200`, setting the relative rate of strange-quark to up/down-quark pair production in string breaking.

To obtain the space-time information required for coalescence afterburners, the production vertices of both partons and hadrons were stored, providing access to the space-time coordinates of nucleon emission needed to evaluate the size of the particle-emitting source. Finally, to prevent feeddown from late weak decays contaminating the primary particle sample used in the analysis, several long-lived hadrons were set as stable, namely the (anti)neutron, the Λ, Σ and Ω (anti)baryons, the kaons and the pions. In contrast, short-lived resonances decaying strongly or electromagnetically, such as the ρ mesons and the Δ baryons, were left free to decay, as their decay products are produced promptly and

close to the primary vertex. Notably, the nucleons that originate from strong decays are produced with timescales of the resonance lifetimes, $\mathcal{O}$(1-10 fm), hence they are available for coalescence.

For the analysis of the presented thesis, the result of `PYTHIA` event generation is stored in the form of a `ROOT` [32] tree, where each *leaf* of the particle *branch* corresponds to an event containing the list of produced particles together with their kinematic information. Only particles that can be detected (i.e. those interacting either strongly or electromagnetically) are saved, thus excluding neutrinos. We also keep out elastically scattered particles and require a specific pseudorapidity range (details in section 5.2).

The algorithm of jet finding is implemented on top of this `PYTHIA` configuration using the `FastJet` package. We adopt in particular the anti-k_t algorithm ($p = -1$) described in section 4.2, with two different radii: $R = 0.4$ and $R = 0.7$. For each event, the list of reconstructed jet four-momenta is stored, where the jet momentum is defined as the sum of all jet-particle momenta. Only jets with momentum $p_T > 5\,\mathrm{GeV/c}$ are accepted. Another branch is added in parallel to the particle one, where a jet index is written for each particle, pointing to the jet it belongs to. The -1 index is used for underlying-event particles. The output tree therefore contains, for each event, the particle list, the jet four-momenta and the particle-to-jet association.

5.1.2 Coalescence afterburner configuration

Protons and neutrons produced by `PYTHIA`-simulated pp collisions are then passed as input to the coalescence afterburner algorithm, giving deuteron p_T-spectra as output. In this analysis, we use the Argonne v_{18} and the N^{4}LO χEFT wavefunctions. The source size, i.e. the width of the assumed Gaussian distribution, is kept fixed to the value of 1 fm. This value should not be interpreted as a precise determination of the emission source, but as a representative scale motivated by femtoscopic measurements in pp collisions at the LHC [15]. Such measurements indicate source radii of the order of 1 fm, comparable to the proton size, although the extracted values depend on event multiplicity and pair transverse momentum. No direct femtoscopic constraint on the source size inside jets is currently available. We therefore adopt the same fixed value for the in-jet and out-of-jet components, providing a common spatial baseline and allowing differences associated with nucleon momentum correlations and jet selection to be studied without introducing different source assumptions. A dedicated investigation of the dependence on the source parametrisation, including its possible m_{T} dependence and distinct in-jet and out-of-jet hypotheses, is left for future work. We have not adopted the thermal-model-based tune (see section 4.3) to correct the fraction of prompt and feeddown nucleons from `PYTHIA`, because it has never been validated for jet-associated production. Moreover, the underlying assumptions of the thermal model, namely that the light hadrons stem from a source in partial equilibrium where quantum numbers are conserved over a limited correlation volume, may not be applicable to production in jets by fragmentation.

The first step of the study was carried out with a sample of 10^6 events and simula-

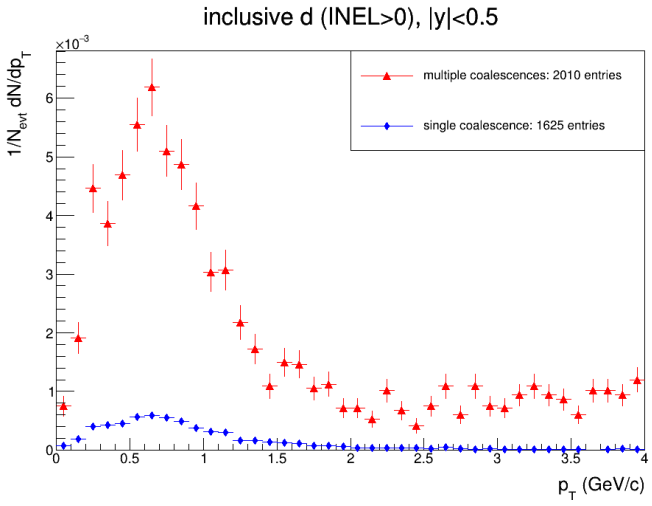


Figure 5.1: Density of deuterons, in units of p_T, obtained by counting all possible coalescences (red curve) or only one of them per nucleon (blue curve).

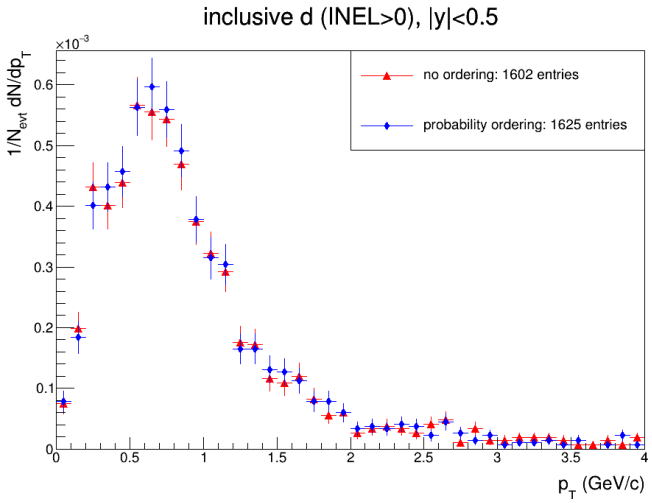


Figure 5.2: Density of deuterons, in units of p_T, obtained by choosing randomly one possible coalescence (red curve) per nucleon or by introducing a probability ordering (blue curve).

tions were analysed in the inclusive case, namely without distinguishing between in-jet and out-of-jet particles. This first configuration allowed to test some aspects of the coalescence algorithm as developed in the employed afterburner. Following these tests, the corresponding chosen configurations were implemented in the afterburner, providing a contribution to the development of the tool itself, which stays beyond the work presented in this thesis.

More specifically, the first question we tested is whether a nucleon could in principle coalesce with more than one other nucleon. We verified that this is possible. Figure 5.1 shows the deuteron p_T-spectra obtained in the case in which we count all possible coalescences (red) or if we allow only one coalescence per nucleon (blue). The fraction of multiple coalescences is about 20%.

A second open point that we addressed with an original implementation for this work is the choice of the nucleon pair, in the case in which one of them can coalesce also with other nucleons. We introduce here a probability ordering, so that we privilege nucleon

pairs with higher coalescence probability. We verified that this approach does not produce a significantly different spectrum (fig.5.2), within the statistical uncertainty, with respect to the random choice of one possible coalescence. We then concluded that, in the case of multiple possible coalescences, they are all similarly likely.

In our analysis, we accept only one coalescence per nucleon and adopt the probability ordering.

5.2 In- and out-of-jet particle kinematics

First of all, we analysed the `PYTHIA` output, i.e. the list of outgoing particles together with their kinematic variables and jet index. We studied the transverse momentum (p_T) and rapidity (y) distributions in and out of jets. Particles defined as *in-jet* belong to a `FastJet`-reconstructed jet of any event (jet index different from -1). We have verified that a particle cannot be clustered by `FastJet` in more than one jet per event. Particles defined as *out-of-jet* do not belong to any jet of any event. We refer to these also as the *underlying event*.

Figures 5.3-5.4 show respectively the dN/p_T and dN/dy distributions of in- and out-of-jet particles. They are obtained for two different values of the jet radius ($R = 0.4$, $R = 0.7$) and for two pseudorapidity intervals corresponding to the full kinematical range ($|\eta| < 5$) and to the fiducial acceptance ($|\eta| < 0.9$) of the ALICE detector central barrel (where identification of deuterons is possible).

Momentum distributions (fig.5.3) exhibit an expected exponential behaviour. Above 5 GeV/c there is no underlying event (bottom panel), since all particles are considered as jets. The in-jet spectrum is normalized (as all other in-jet p_T spectra in this chapter) for the number of generated events, unity of p_T, and jet area (computed as πR^2), so that points represent the density of particles per unit of momentum and area in each event. We can notice that small-jet particles keep a higher normalized dN/dp_T, since the anti-k_t algorithm includes softer and softer particles while increasing the jet radius. At fixed radius, the central- and extended-pseudorapidity curves are very similar, except for the number of particles.

Rapidity distributions (Fig.5.4) exhibit a nearly constant shape, with different kinds of border effects. All curves decrease smoothly towards their endpoints, due to the discrepancy between rapidity and pseudorapidity for low-energy particles. This is particularly evident in $|\eta| < 0.9$ distributions (magenta and green), where a cut applied to a flat plateau appears smeared. At $y \sim 5$, the decrease is also given by physical reasons. Here indeed, the production of particles becomes rarer as approaching the beam, due to energy and momentum conservation. Finally, jet particles (top panel) show an additional geometrical border effect. If part of the jet falls out of the acceptance, some jet particles are lost, thus moving the knee at a distance of about R from the endpoint. This is better seen in the large-radius configuration (blue). The spectrum normalization is the same as in the previous case.

Since our final goal is to study deuteron formation, we extracted the same spectra,

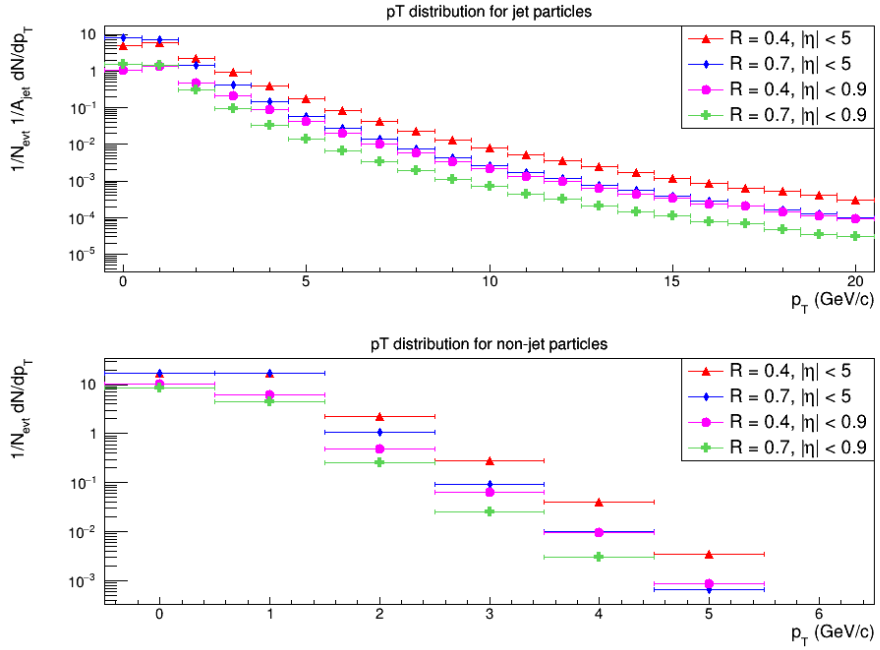


Figure 5.3: p_T distribution of jet (top) and non-jet (bottom) particles in four different $R - \eta$ configurations. Normalized by jet area (only for the top) and number of events.

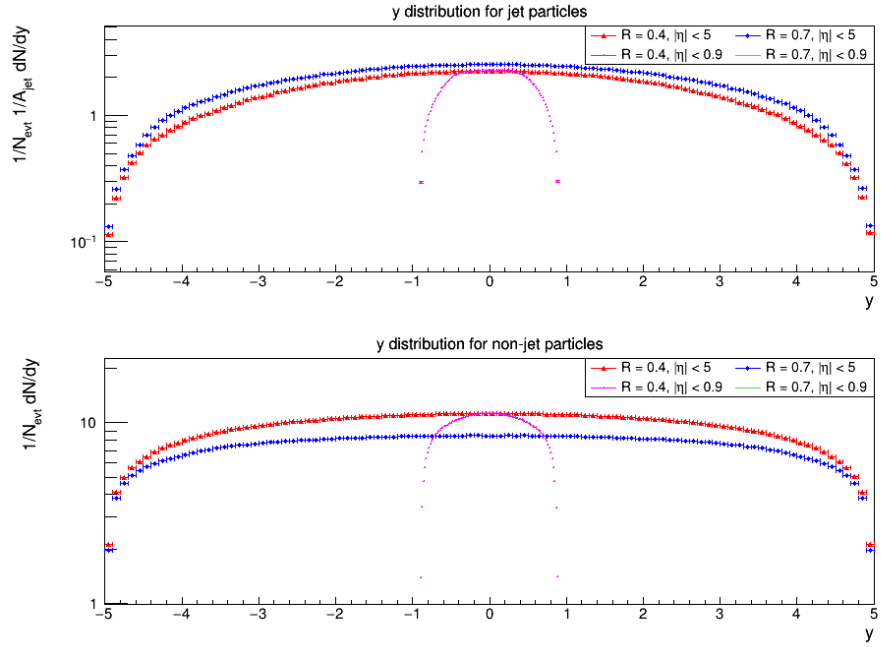


Figure 5.4: y distribution of jet (top) and non-jet (bottom) particles in four different $R - \eta$ configurations. Normalized jet area (only for the top) and number of events.

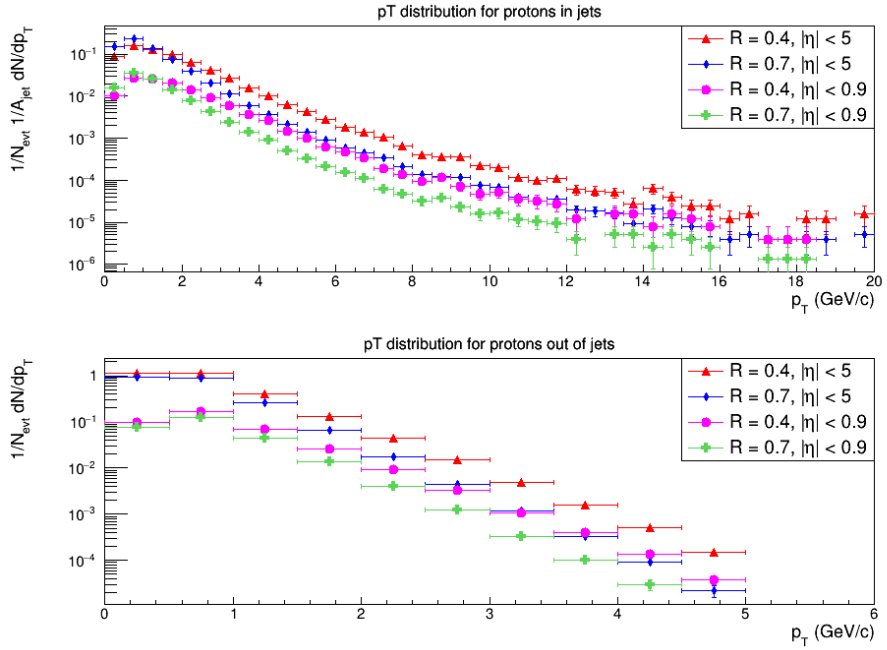


Figure 5.5: p_T distribution of jet (top) and non-jet (bottom) protons in four different $R - \eta$ configurations. Normalized by jet area (only for the top) and number of events.

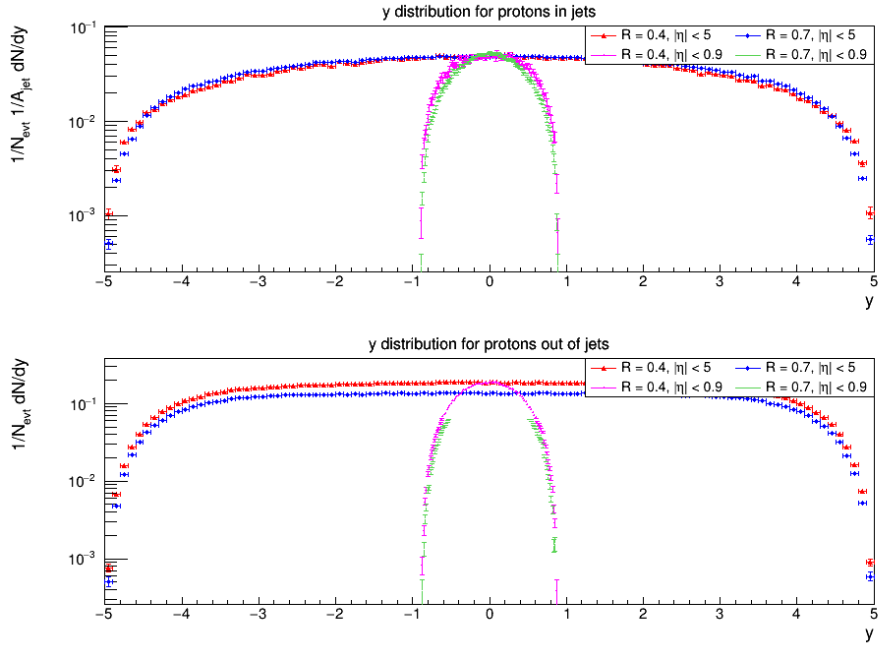


Figure 5.6: y distribution of jet (top) and non-jet (bottom) protons in four different $R - \eta$ configurations. Normalized by jet area (only for the top) and number of events.

isolating the proton contribution. We expect protons and neutrons to be produced in equal amounts at the LHC energies, due to isospin symmetry that holds at high collision energies. The `PYTHIA` event generator also generates the same spectrum for protons and neutrons. A symmetry between particle and antiparticle is also respected by the generator, as observed at the LHC, where the ratio $\bar{p}/p$ is consistent with unity. Protons are identified based on the particle PDG code from the generator.

Unlike the inclusive case, the proton p_T spectrum shows a clear peak around $p_T \simeq 1\,\mathrm{GeV/c}$. This is a mass effect due to thermal hadron production. For y distributions, the curves in the same pseudorapidity interval are less separated than in the inclusive case. This could suggest that protons are produced close to the jet core: widening the jet radius predominantly captures soft hadrons, so the relative gain in proton yield would be smaller than the corresponding gain in the inclusive yield. This core production of protons could be explained by the Lund String Model [50].

5.3 In- and out-of-jet deuteron production

At this point, we applied the coalescence afterburner to protons and neutrons in order to obtain the p_T deuteron spectrum. In these studies, we increased the sample by generating 10^7 pp collisions at $\sqrt{s} = 13.6\,\mathrm{TeV}$. All following spectra are obtained at midrapidity ($|y| < 0.5$) and normalized to the event class INEL > 0. We keep the distinction between two different values for the jet radius ($R = 0.4,\ 0.7$).

The results obtained using the Argonne v_{18} wavefunction are shown in Fig.5.7. The yield of deuterons in jets shows an expected increase with a larger radius R. Moreover, the peak is shifted at larger p_T in jets, and particularly in the $R = 0.4$ case, being more collimated objects with respect to the underlying event or to larger jets including more

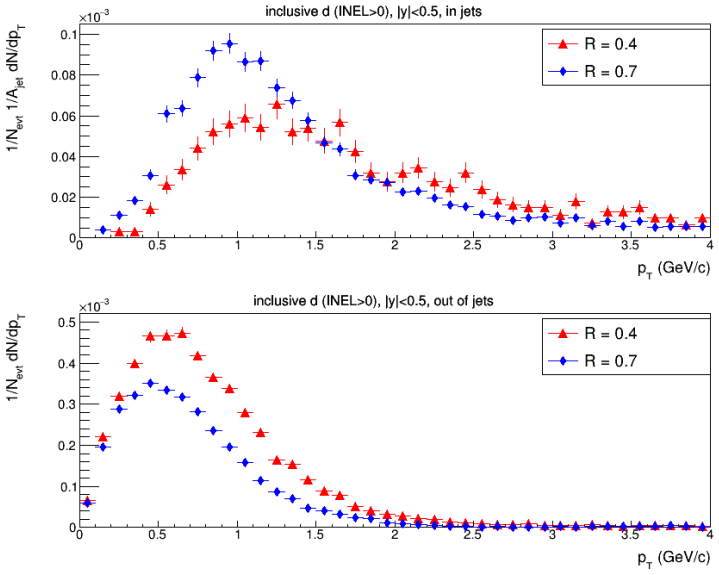


Figure 5.7: p_T spectra for jet (top) and non-jet (bottom) deuterons in the two used jet radii. Normalized by unity of momentum, jet area (only for the top) and number of events.

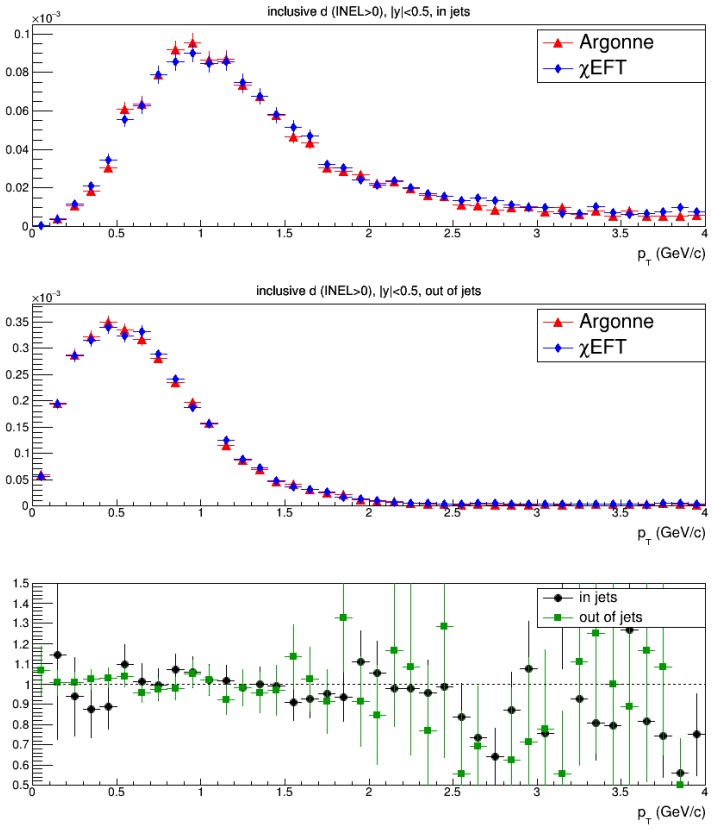


Figure 5.8: Superposition of deuteron spectra from Argonne v_{18} and χEFT both in (top) and out (middle) of jets, for the $R = 0.7$ configuration. In the bottom panel, the ratio between the two spectra is reported.

soft particles. Predicted mean transverse momenta are reported in Tab.5.1.

	$R = 0.4$	$R = 0.7$
Mean p_T in jets	1.72 ± 0.02	1.37 ± 0.01
Mean p_T in UE	0.825 ± 0.005	0.720 ± 0.005

Table 5.1: Mean transverse momenta of in- and out-of-jet deuteron spectra for the two R options, as predicted by our model. Values are provided in GeV/c.

The jet radius does not modify the shape of the underlying-event spectra, but only the yield, increasing of 52% with $R = 0.7$ with respect to the $R = 0.4$ case. We also verified that results obtained with the χEFT wavefunction are consistent within our uncertainties. Figure 5.8 compares results obtained with the two wavefunctions, both in and out of jets, together with the ratio. Despite statistical fluctuations, the ratio is compatible with unity in the full analyzed p_T range. The two wavefunctions are actually different at short relative distance (see Fig. 8 in[46]); the compatibility of our results could signal that our model is not sensitive to this regime. In the following, we will only show the Argonne wavefunction results.

In addition to the inclusive case, we also extracted the deuteron distributions for each of the four possible combinations of prompt and feeddown protons and neutrons. They

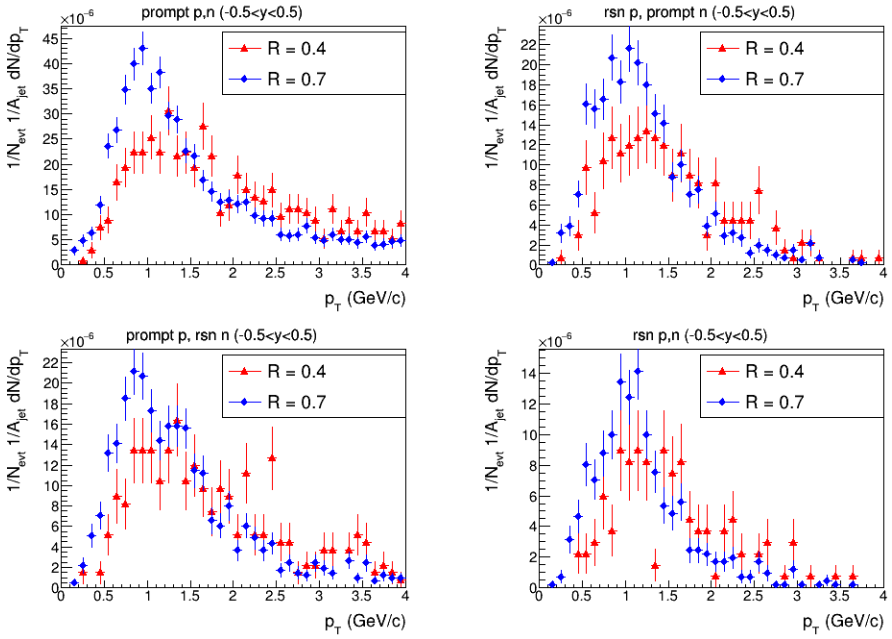


Figure 5.9: Deuteron spectra obtained in the four prompt-feeddown classes in jets. Results are shown for both jet radii and normalized by the number of events and jet area.

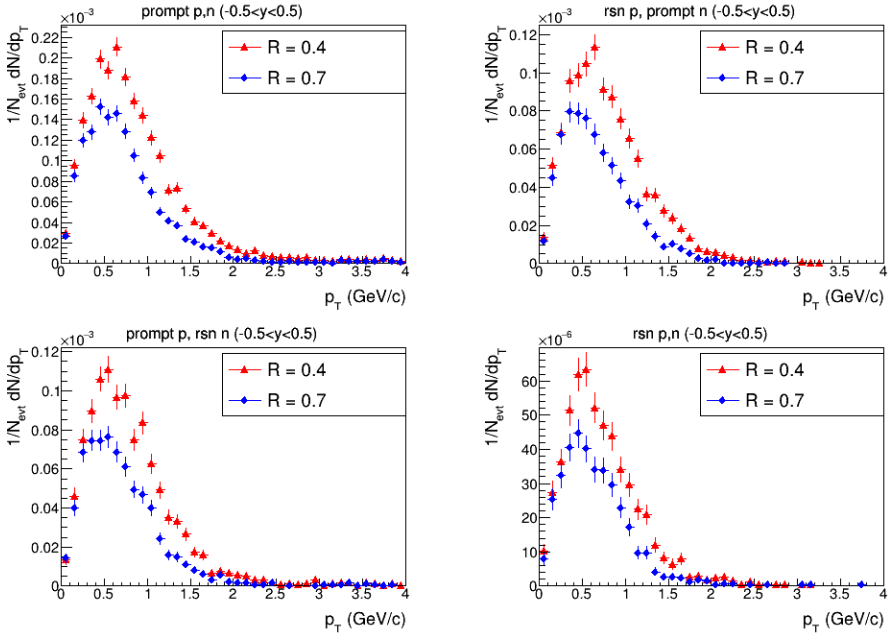


Figure 5.10: Deuteron spectra obtained in the four prompt-feeddown classes out of jets. Results are shown for both jet radii and normalized by the number of events.

are shown in Fig.5.9 for jets and Fig.5.10 for the underlying event. In the jet case, similar yields are obtained in the four classes with the same shape as in the inclusive case. As expected, the most populated one is the prompt-prompt class, which is a factor of about two larger than the prompt-resonance case and a factor of about three larger than the resonance-resonance case. For the underlying event, the yield is one order of magnitude greater for all classes, with respect to the in-jet case, except for the resonance-resonance one. We thus understand that the coalescence mechanism favours prompt nucleons because feeddown ones are produced late, after the resonance decay. The resonance-resonance class is therefore especially suppressed compared to the other combinations. We observe that the hierarchy between the two jet-radius values is the same as in the inclusive case.

In all previous studies, we summed up contributions from all jet particles without considering to which jet they belong. However, we also verified explicitly that deuterons can also be formed by nucleons belonging to different jets or by a jet nucleon and one from the UE. The fractions of each possible combination of coalescing nucleon pair, depending on the jet-associated or underlying-event production of nucleons, are summarized in Tab.5.2.

	$R = 0.4$	$R = 0.7$
Same jet	0.08	0.26
Different jets	0.01	0.04
Jet-UE	0.08	0.15
Both UE	0.83	0.55

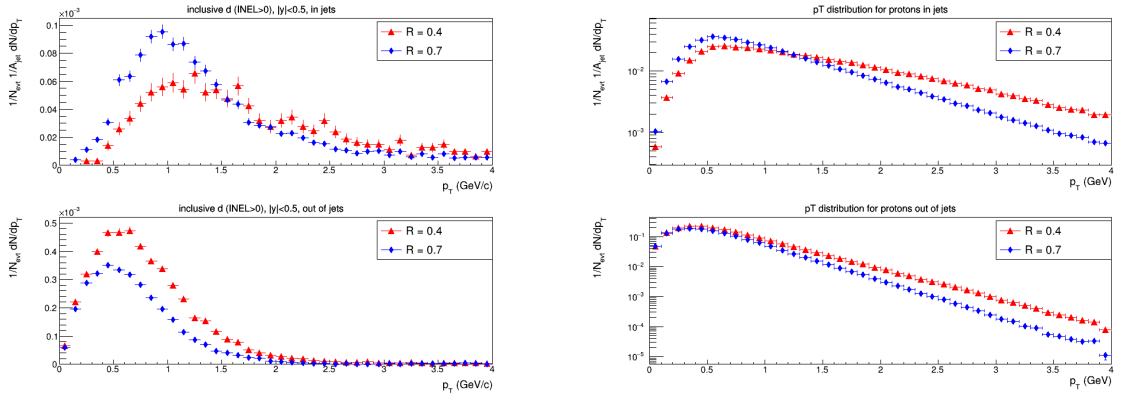
Table 5.2: Fraction of nucleon pairs undergoing coalescence, based on the jet or UE origin of nucleons.

Coalescence of nucleons from different jets is kinematically suppressed, especially for smaller jets. The majority of deuterons comes from UE nucleons, despite the collimation of particles in jets, which should favour the coalescence process because jets intrinsically implement the spatial-proximity constraint. However, we notice that the underlying event also contains the majority of nucleons with respect to the whole event yield. This is the reason why we move forward by comparing the production in terms of coalescence probability rather than the absolute number of deuterons.

The coalescence parameter (see section 3.3) is computed as

$$B_2 = \left(\frac{1}{2\pi P_T}\frac{dN_d}{dP_T}\right) \Big/ \left(\frac{1}{2\pi p_T^p}\frac{dN_p}{dp_T^p}\right)^2 \tag{5.1}$$

where the numerator and denominator, i.e. the deuteron and proton spectra, are shown in Fig.5.11. The proton yield is squared to account also for the neutron component under the assumption previously discussed that p and n productions are the same at this energy. The B_2 is given as a function of the proton transverse momentum, taken as half of that of the deuteron one. Figure 5.12 shows the results obtained in and out of jets for the two jet radii. An expected one-order-of-magnitude enhancement of B_2 in jets is predicted. In particular, we understand this to be mostly due to momentum correlations, since the source size



(a) (b)

Figure 5.11: a) p_T spectra for jet (top) and non-jet (bottom) deuterons in the two used jet radii, used for the computation of B_2. b) p_T spectra for jet (top) and non-jet (bottom) protons in the two used jet radii, used for the computation of B_2. All spectra are normalized by jet area (only for the top ones) and number of events.

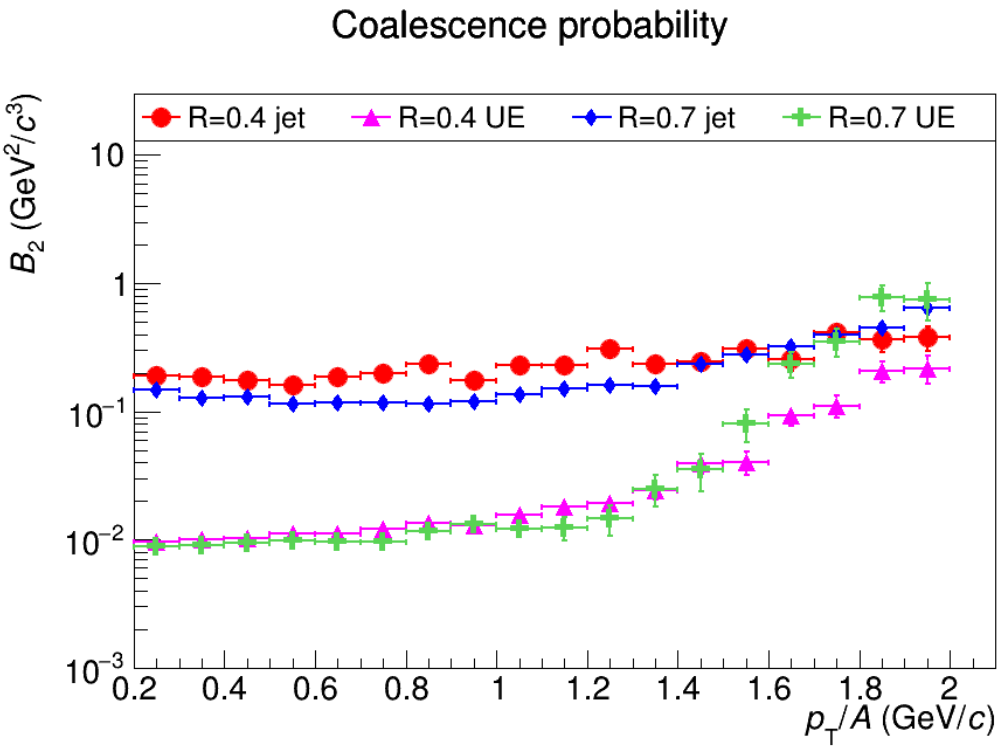


Figure 5.12: Coalescence parameter B_2, computed as a function of p_T/A, according to eq.(5.1). Both jet and UE values are shown for the two different jet radii. Systematic uncertainties are due to the input spectra bin width.

imposed by the afterburner is the same in jets and UE. Points up to $p_T/A \simeq 1.2-1.4\,\mathrm{GeV/c}$ are in quantitative agreement with ALICE measurements in pp collisions at $\sqrt{s} = 13\,\mathrm{TeV}$, shown in Fig.2.7. It has to be noted, however, that in the ALICE data, the selection of in-jet/out-of-jet was based on an azimuthal-angle-based definition of the Towards and Transverse region, whereas data based on a full-jet reconstruction using `FastJet` are not available at present. The comparison between our predictions and ALICE results is thus limited by a different jet definition. We can still conclude that the hierarchy in B_2 between jets and underlying event is reproduced. Above $p_T/A \simeq 1.4\,\mathrm{GeV/c}$, our model predicts an increase of B_2, in particular in the underlying event, where we reach about the same values as in jets. A qualitatively similar dependence on p_T was observed in inelastic pp collisions at $\sqrt{s} = 7\,\mathrm{TeV}$ without any selection on the event multiplicity [10], nor any jet/UE distinction. In that case, the rise with p_T was partially attributed to the hardening of the proton spectrum with increasing multiplicity, which is "hidden" in the minimum bias event selection. Based on this, we could speculate that the increase with p_T in the UE B_2 may arise from a multiplicity-dependent hardening of the UE nucleon spectra that is "hidden" in the multiplicity-integrated sample considered here. A future multiplicity-dependent study of proton production, separating also in-jet and UE production, may further clarify this point.

Finally, some systematic variations should be implemented in order to fully validate the model. In particular, this would include varying the prompt/resonance nucleon components in jets and the underlying event or computing the rescaling factor needed to reproduce ALICE results; exploring other options for the source size, such as using the native source distribution or the values tuned to ALICE data; investigating the possibility that a deuteron could bind another nucleon to form tritium or helium.

Conclusions

This work was motivated by the interest in studying (anti)deuteron production in- and out-of-jet in pp collisions at LHC energies. To this end, we established a simulation chain that can be used to predict the production of deuterons for comparison to ALICE data. We used `PYTHIA 8.3` Monte Carlo generator to simulate pp collisions at $\sqrt{s} = 13.6$ TeV. We employ the anti-k_t sequential recombination algorithm implemented by the `FastJet` package to define the jets, using values of $R = 0.4$, 0.7 for the jet radius together with a minimum momentum threshold fixed at $p_T = 5\,\mathrm{GeV}/c$. In the storage of the event output, we retain particle-to-jet associations and jet energies, in addition to particle kinematics. We then provide this data as input to the coalescence afterburner, focusing on the midrapidity region ($|y| < 0.5$), which coincides with the kinematical region explored by the ALICE experiment. In this model, the deuteron formation probability is obtained by the superposition of deuteron and proton-neutron pairs Wigner functions. The deuteron wave function was modelled based alternatively on the Argonne v_{18} potential and on a ($\mathrm{N^4LO}$) chiral effective field theory parametrization, verifying the compatibility of these two descriptions within the uncertainties. We checked the possibility of multiple coalescences for the same nucleon, finding that about 20% of them could in principle coalesce with more than one nucleon. We then required at most one coalescence per nucleon, introducing a probability ordering in order to favour more probable ones. In the analysis of the resulting deuteron p_T spectra, we observe a larger mean transverse momentum in jets with respect to the underlying event.

We also distinguished four classes based on the prompt or feeddown origin of nucleons. Deuteron p_T distributions are qualitatively similar in the four cases, both for jets and the underlying event, with one order-of-magnitude suppression in yield for the resonance-resonance case with respect to the prompt-prompt one. We verified that deuterons can also form from different-jet nucleons or from a jet nucleon and one from the underlying event. These pairings occur in about 9% of the cases for $R = 0.4$ and 19% for $R = 0.7$.

Finally, we computed the coalescence parameter B_2 in and out of jets. We found an order-of-magnitude enhancement of B_2 in jets compared to the underlying event, together with a slight increase for smaller jets. The B_2 is approximately p_T-independent up to $p_T/A \simeq 1.2 - 1.4\,\mathrm{GeV}/c$, where it starts increasing, especially in the underlying event. These results, in particular the hierarchy of B_2, are consistent with ALICE measurements, available up to $p_T/A \simeq 1.4\,\mathrm{GeV}/c$. The comparison is nevertheless limited by the different definitions of jet-associated and underlying-event production and by the present absence

of a systematic variation of the source and generator settings. The rise of the B_2 for $p_T/A > 1.4\,\mathrm{GeV}/c$ could be regarded as a testable model prediction shall new data become available in this kinematic range.

This work contributes to the CosmicAntinuclei project, which aims to constrain coalescence models and improve the predictions for signal and background rates of light antinuclei originating from dark matter interactions. This jet analysis offers a new point of view in the context of nucleus formation, and provides at the same time a first qualitative benchmark of the simulation chain employed and new predictions to be compared with future experimental results.

Bibliography

[1] K. Aamodt et al. "The ALICE experiment at the CERN LHC". In: *JINST* 3 (2008), S08002. DOI: 10.1088/1748-0221/3/08/S08002.

[2] K. Abe et al. "Search for Antihelium with the BESS-Polar Spectrometer". In: *Phys. Rev. Lett.* 108 (13 2012), p. 131301. DOI: 10.1103/PhysRevLett.108.131301. URL: https://link.aps.org/doi/10.1103/PhysRevLett.108.131301.

[3] S. Acharya et al. "Observation of deuteron and antideuteron formation from resonance-decay nucleons". In: *Nature* 648.8093 (2025), pp. 306–311. DOI: 10.1038/s41586-025-09775-5. arXiv: 2504.02393 [nucl-ex].

[4] S. and Acharya et al. "The ALICE experiment: a journey through QCD". In: *The European Physical Journal C* 84.8 (Aug. 2024). ISSN: 1434-6052. DOI: 10.1140/epjc/s10052-024-12935-y. URL: http://dx.doi.org/10.1140/epjc/s10052-024-12935-y.

[5] Shreyasi Acharya et al. "ALICE upgrades during the LHC Long Shutdown 2". In: *JINST* 19.05 (2024), P05062. DOI: 10.1088/1748-0221/19/05/P05062. arXiv: 2302.01238 [physics.ins-det].

[6] Shreyasi Acharya et al. "Enhanced Deuteron Coalescence Probability in Jets". In: *Phys. Rev. Lett.* 131.4 (2023), p. 042301. DOI: 10.1103/PhysRevLett.131.042301. arXiv: 2211.15204 [nucl-ex].

[7] Shreyasi Acharya et al. "First Observation of an Attractive Interaction between a Proton and a Cascade Baryon". In: *Phys. Rev. Lett.* 123.11 (2019), p. 112002. DOI: 10.1103/PhysRevLett.123.112002. arXiv: 1904.12198 [nucl-ex].

[8] Shreyasi Acharya et al. "Jet-associated deuteron production in pp collisions at s=13 TeV". In: *Phys. Lett. B* 819 (2021), p. 136440. DOI: 10.1016/j.physletb.2021.136440. arXiv: 2011.05898 [nucl-ex].

[9] Shreyasi Acharya et al. "Measurement of anti-^{3}He nuclei absorption in matter and impact on their propagation in the Galaxy". In: *Nature Phys.* 19.1 (2023), pp. 61–71. DOI: 10.1038/s41567-022-01804-8. arXiv: 2202.01549 [nucl-ex].

[10] Shreyasi Acharya et al. "Multiplicity dependence of (anti-)deuteron production in pp collisions at $\sqrt{s} = 7$ TeV". In: *Phys. Lett. B* 794 (2019), pp. 50–63. DOI: 10.1016/j.physletb.2019.05.028. arXiv: 1902.09290 [nucl-ex].

[11] Shreyasi Acharya et al. "Multiplicity dependence of light-flavor hadron production in pp collisions at $\sqrt{s} = 7$ TeV". In: *Phys. Rev. C* 99.2 (2019), p. 024906. DOI: 10.1103/PhysRevC.99.024906. arXiv: 1807.11321 [nucl-ex].

[12] Shreyasi Acharya et al. "p-p, p-Λ and Λ-Λ correlations studied via femtoscopy in pp reactions at $\sqrt{s} = 7$ TeV". In: *Phys. Rev. C* 99.2 (2019), p. 024001. DOI: 10.1103/PhysRevC.99.024001. arXiv: 1805.12455 [nucl-ex].

[13] Shreyasi Acharya et al. "Production of light (anti)nuclei in pp collisions at $\sqrt{s} =$ 13 TeV". In: *JHEP* 01 (2022), p. 106. DOI: 10.1007/JHEP01(2022)106. arXiv: 2109.13026 [nucl-ex].

[14] Shreyasi Acharya et al. "Search for a common baryon source in high-multiplicity pp collisions at the LHC". In: *Phys. Lett. B* 811 (2020). [Erratum: Phys.Lett.B 861, 139233 (2025)], p. 135849. DOI: 10.1016/j.physletb.2020.135849. arXiv: 2004.08018 [nucl-ex].

[15] Shreyasi Acharya et al. "Search for a common baryon source in high-multiplicity pp collisions at the LHC". In: *Phys. Lett. B* 811 (2020). [Erratum: Phys.Lett.B 861, 139233 (2025)], p. 135849. DOI: 10.1016/j.physletb.2020.135849. arXiv: 2004.08018 [nucl-ex].

[16] Jaroslav Adam et al. "One-dimensional pion, kaon, and proton femtoscopy in Pb-Pb collisions at $\sqrt{s_{\rm NN}}$ =2.76 TeV". In: *Phys. Rev. C* 92.5 (2015), p. 054908. DOI: 10.1103/PhysRevC.92.054908. arXiv: 1506.07884 [nucl-ex].

[17] Jaroslav Adam et al. "Production of light nuclei and anti-nuclei in pp and Pb-Pb collisions at energies available at the CERN Large Hadron Collider". In: *Phys. Rev. C* 93.2 (2016), p. 024917. DOI: 10.1103/PhysRevC.93.024917. arXiv: 1506.08951 [nucl-ex].

[18] C. Adler et al. "Antideuteron production in Au + Au collisions at $\sqrt{s_{NN}} = 130$ GeV". In: *Phys. Rev. C* 64 (2001), p. 054908. DOI: 10.1103/PhysRevC.64.054908.

[19] Y. Ajima et al. "A superconducting solenoidal spectrometer for a balloon borne experiment". In: *Nucl. Instrum. Meth. A* 443 (2000), pp. 71–100. DOI: 10.1016/S0168-9002(99)01010-4.

[20] Dana Ali Hassan Abdallah et al. "Deuteron coalescence probability in jets in p-Pb collisions at $\sqrt{s_{\rm NN}} = 5.02$ TeV". In: (Feb. 2026). arXiv: 2602.22880 [nucl-ex].

[21] ALICE Collaboration. "Measurement of the Low-Energy Antideuteron Inelastic Cross Section". In: *Physical Review Letters* 125.16 (Oct. 2020). ISSN: 1079-7114. DOI: 10.1103/physrevlett.125.162001. URL: http://dx.doi.org/10.1103/PhysRevLett.125.162001.

[22] J. Altmann et al. "Towards the understanding of heavy quarks hadronization: from leptonic to heavy-ion collisions". In: *The European Physical Journal C* 85.1 (Jan. 2025). ISSN: 1434-6052. DOI: 10.1140/epjc/s10052-024-13641-5. URL: http://dx.doi.org/10.1140/epjc/s10052-024-13641-5.

[23] Javira Altmann and Peter Skands. "String junctions revisited". In: *JHEP* 07 (2024), p. 238. DOI: 10.1007/JHEP07(2024)238. arXiv: 2404.12040 [hep-ph].

[24] AMS Collaboration. "The Alpha Magnetic Spectrometer (AMS) on the international space station: Part II — Results from the first seven years". In: *Physics Reports* 894 (2021), pp. 1–116. DOI: 10.1016/j.physrep.2020.09.003.

[25] AMS Collaboration. "Towards Understanding the Origin of Cosmic-Ray Positrons". In: *Phys. Rev. Lett.* 122 (4 Jan. 2019), p. 041102. DOI: 10.1103/PhysRevLett.122.041102. URL: https://link.aps.org/doi/10.1103/PhysRevLett.122.041102.

[26] Carl D. Anderson. "The Apparent Existence of Easily Deflectable Positives". In: *Science* 76 (1932), pp. 238–239. DOI: 10.1126/science.76.1967.238.

[27] F. Becattini. "An Introduction to the Statistical Hadronization Model". In: *International School on Quark-Gluon Plasma and Heavy Ion Collisions: past, present, future*. Jan. 2009. arXiv: 0901.3643 [hep-ph].

[28] Francesca Bellini and Alexander P. Kalweit. "Testing production scenarios for (anti-)(hyper-)nuclei and exotica at energies available at the CERN Large Hadron Collider". In: *Phys. Rev. C* 99 (5 2019), p. 054905. DOI: 10.1103/PhysRevC.99.054905. URL: https://link.aps.org/doi/10.1103/PhysRevC.99.054905.

[29] Francesca Bellini et al. "Examination of coalescence as the origin of nuclei in hadronic collisions". English. In: *Physical Review C* 103.1 (2021). ISSN: 2469-9985. DOI: 10.1103/PhysRevC.103.014907.

[30] Christian Bierlich et al. "A comprehensive guide to the physics and usage of PYTHIA 8.3". In: *SciPost Phys. Codeb.* 2022 (2022), p. 8. DOI: 10.21468/SciPostPhysCodeb.8. arXiv: 2203.11601 [hep-ph].

[31] Mathieu Boudaud et al. "AMS-02 antiprotons' consistency with a secondary astrophysical origin". In: *Phys. Rev. Res.* 2.2 (2020), p. 023022. DOI: 10.1103/PhysRevResearch.2.023022. arXiv: 1906.07119 [astro-ph.HE].

[32] R. Brun and F. Rademakers. "ROOT: An object oriented data analysis framework". In: *Nucl. Instrum. Meth. A* 389 (1997). Ed. by M. Werlen and D. Perret-Gallix, pp. 81–86. DOI: 10.1016/S0168-9002(97)00048-X.

[33] S. T. Butler and C. A. Pearson. "Deuterons from High-Energy Proton Bombardment of Matter". In: *Phys. Rev.* 129 (2 1963), pp. 836–842. DOI: 10.1103/PhysRev.129.836. URL: https://link.aps.org/doi/10.1103/PhysRev.129.836.

[34] Matteo Cacciari, Gavin P Salam, and Gregory Soyez. "The anti-k$_t$*jetclusteringalgorithm*". In: *Journal of High Energy Physics* 2008.04 (Apr. 2008), pp. 063–063. ISSN: 1029-8479. DOI: 10.1088/1126-6708/2008/04/063. URL: http://dx.doi.org/10.1088/1126-6708/2008/04/063.

[35] Matteo Cacciari, Gavin P. Salam, and Gregory Soyez. "FastJet user manual: (for version 3.0.2)". In: *The European Physical Journal C* 72.3 (Mar. 2012). ISSN: 1434-6052. DOI: 10.1140/epjc/s10052-012-1896-2. URL: http://dx.doi.org/10.1140/epjc/s10052-012-1896-2.

[36] Jesper R. Christiansen and Peter Z. Skands. "String Formation Beyond Leading Colour". In: *JHEP* 08 (2015), p. 003. DOI: 10.1007/JHEP08(2015)003. arXiv: 1505.01681 [hep-ph].

[37] Richard Corke and Torbjörn Sjöstrand. "Interleaved Parton Showers and Tuning Prospects". In: *JHEP* 03 (2011), p. 032. DOI: 10.1007/JHEP03(2011)032. arXiv: 1011.1759 [hep-ph].

[38] D. E. Dorfan et al. "Observation of antideuterons". In: *Phys. Rev. Lett.* 14 (1965), pp. 1003–1006. DOI: 10.1103/PhysRevLett.14.1003.

[39] D. R. Entem, R. Machleidt, and Y. Nosyk. "High-quality two-nucleon potentials up to fifth order of the chiral expansion". In: *Phys. Rev. C* 96 (2 2017), p. 024004. DOI: 10.1103/PhysRevC.96.024004. URL: https://link.aps.org/doi/10.1103/PhysRevC.96.024004.

[40] K. Freese. "Review of Observational Evidence for Dark Matter in the Universe and in upcoming searches for Dark Stars". In: *EAS Publications Series* 36 (2009), pp. 113–126. ISSN: 1638-1963. DOI: 10.1051/eas/0936016. URL: http://dx.doi.org/10.1051/eas/0936016.

[41] Diego-Mauricio Gomez-Coral et al. "Deuteron and Antideuteron Production Simulation in Cosmic-Ray Interactions". In: *Phys. Rev. D* 98.2 (2018), p. 023012. DOI: 10.1103/PhysRevD.98.023012. arXiv: 1806.09303 [astro-ph.HE].

[42] Ulrich Heinz and Barbara V. Jacak. "Two particle correlations in relativistic heavy ion collisions". In: *Annual Review of Nuclear and Particle Science* 49.1 (Dec. 1999), pp. 529–579. ISSN: 1545-4134. DOI: 10.1146/annurev.nucl.49.1.529. URL: http://dx.doi.org/10.1146/annurev.nucl.49.1.529.

[43] M. Kachelrieß, S. Ostapchenko, and J. Tjemsland. "Alternative coalescence model for deuteron, tritium, helium-3 and their antinuclei". In: *Eur. Phys. J. A* 56.1 (2020), p. 4. DOI: 10.1140/epja/s10050-019-00007-9. arXiv: 1905.01192 [hep-ph].

[44] Michael Annan Lisa et al. "Femtoscopy in relativistic heavy ion collisions". In: *Ann. Rev. Nucl. Part. Sci.* 55 (2005), pp. 357–402. DOI: 10.1146/annurev.nucl.55.090704.151533. arXiv: nucl-ex/0505014.

[45] Leif Lönnblad and Harsh Shah. "Baryon correlations in Pythia". In: *Eur. Phys. J. C* 83.12 (2023), p. 1105. DOI: 10.1140/epjc/s10052-023-12271-7. arXiv: 2309.01557 [hep-ph].

[46] Maximilian Mahlein et al. "A realistic coalescence model for deuteron production". In: *Eur. Phys. J. C* 83.9 (2023), p. 804. DOI: 10.1140/epjc/s10052-023-11972-3. arXiv: 2302.12696 [hep-ex].

[47] T. Massam et al. “Experimental observation of antideuteron production”. In: *Nuovo Cimento Serie* 39.1 (Sept. 1965), pp. 10–14. DOI: 10.1007/BF02814251.

[48] S. Mrówczyński. “Enhancement of Deuteron Production in Jets”. In: *Acta Physica Polonica B* 55.6 (2024), p. 1. ISSN: 1509-5770. DOI: 10.5506/aphyspolb.55.6-a2. URL: http://dx.doi.org/10.5506/APhysPolB.55.6-A2.

[49] S. Navas et al. “Review of Particle Physics”. In: *Phys. Rev. D* 110 (3 Aug. 2024), p. 030001. DOI: 10.1103/PhysRevD.110.030001. URL: https://link.aps.org/doi/10.1103/PhysRevD.110.030001.

[50] Antonio Ortiz and Robert Vertesi. “Baryon enhancement in jets”. In: (Apr. 2026). arXiv: 2604.23189 [hep-ph].

[51] P. Picozza et al. “PAMELA: A Payload for Antimatter Matter Exploration and Light-nuclei Astrophysics”. In: *Astropart. Phys.* 27 (2007), pp. 296–315. DOI: 10.1016/j.astropartphys.2006.12.002. arXiv: astro-ph/0608697.

[52] Troy A. Porter, Gudlaugur Johannesson, and V. Igor Moskalenko. “The GALPROP Cosmic-ray Propagation and Nonthermal Emissions Framework: Release v57”. In: *Astrophys. J. Supp.* 262.1 (2022), p. 30. DOI: 10.3847/1538-4365/ac80f6. arXiv: 2112.12745 [astro-ph.HE].

[53] K. Sakai et al. “Search for Antideuterons of Cosmic Origin Using the BESS-Polar II Magnetic-Rigidity Spectrometer”. In: *Phys. Rev. Lett.* 132 (13 2024), p. 131001. DOI: 10.1103/PhysRevLett.132.131001. URL: https://link.aps.org/doi/10.1103/PhysRevLett.132.131001.

[54] Gavin P. Salam. “Towards Jetography”. In: *Eur. Phys. J. C* 67 (2010), pp. 637–686. DOI: 10.1140/epjc/s10052-010-1314-6. arXiv: 0906.1833 [hep-ph].

[55] H. Sato and K. Yazaki. “On the coalescence model for high-energy nuclear reactions”. In: *Phys. Lett. B* 98 (1981), pp. 153–157. DOI: 10.1016/0370-2693(81)90976-X.

[56] Laura Šerkšnytė et al. “Reevaluation of the cosmic antideuteron flux from cosmic-ray interactions and from exotic sources”. In: *Phys. Rev. D* 105.8 (2022), p. 083021. DOI: 10.1103/PhysRevD.105.083021. arXiv: 2201.00925 [astro-ph.HE].

[57] A. Sherstnev and R.S. Thorne. “Parton distributions for LO generators”. In: *The European Physical Journal C* 55.4 (May 2008), pp. 553–575. ISSN: 1434-6052. DOI: 10.1140/epjc/s10052-008-0610-x. URL: http://dx.doi.org/10.1140/epjc/s10052-008-0610-x.

[58] Peter Zeiler Skands, Stefano Carrazza, and Juan Rojo. “Tuning PYTHIA 8.1: the Monash 2013 Tune”. In: *Eur. Phys. J. C* 74.8 (2014), p. 3024. DOI: 10.1140/epjc/s10052-014-3024-y. arXiv: 1404.5630 [hep-ph].

[59] Maurizio Spurio. *Probes of Multimessenger Astrophysics. Charged cosmic rays, neutrinos, γ-rays and gravitational waves*. Astronomy and Astrophysics Library. Springer, 2018. ISBN: 978-3-319-96853-7. DOI: 10.1007/978-3-319-96854-4.

[60] STAR Collaboration, B. I. Abelev, et al. "Observation of an Antimatter Hypernucleus". In: *Science* 328 (2010), pp. 58–62. DOI: 10.1126/science.1183980. arXiv: 1003.2030 [nucl-ex].

[61] STAR Collaboration, H. Agakishiev, et al. "Observation of the antimatter helium-4 nucleus". In: *Nature* 473 (2011). [Erratum: Nature 475, 412 (2011)], pp. 353–356. DOI: 10.1038/nature10079. arXiv: 1103.3312 [nucl-ex].

[62] Samuel C. C. Ting. *Latest Results from the AMS Experiment on the International Space Station*. Colloquium, CERN. Unpublished presentation. May 2018.

[63] Virginia Trimble. "Existence and Nature of Dark Matter in the Universe". In: *Ann. Rev. Astron. Astrophys.* 25 (1987), pp. 425–472. DOI: 10.1146/annurev.aa.25.090187.002233.

[64] Volodymyr Vovchenko and Horst Stoecker. "Thermal-FIST: A package for heavy-ion collisions and hadronic equation of state". In: *Comput. Phys. Commun.* 244 (2019), pp. 295–310. DOI: 10.1016/j.cpc.2019.06.024. arXiv: 1901.05249 [nucl-th].

[65] R. B. Wiringa, V. G. J. Stoks, and R. Schiavilla. "Accurate nucleon-nucleon potential with charge-independence breaking". In: *Phys. Rev. C* 51 (1 1995), pp. 38–51. DOI: 10.1103/PhysRevC.51.38. URL: https://link.aps.org/doi/10.1103/PhysRevC.51.38.

[66] Fritz Zwicky. "Die Rotverschiebung von extragalaktischen Nebeln". In: *Helvetica Physica Acta* 6 (1933). English translation by H. Andernach, arXiv:1711.01693, pp. 110–127.